Mehmani Ayaz (Orcid ID: 0000-0002-9193-1817)

Balhoff Matthew (Orcid ID: 0000-0001-7615-1946)

Torres-Verdin Carlos (Orcid ID: 0000-0001-6628-4833)

Microfluidic diagnostics of the impact of local microfracture connectivity on hydrocarbon recovery following water injection

Yujing Du[1], Ayaz Mehmani[*1], Ke Xu[2], Shaina Kelly[3], Matthew Balhoff[1] and Carlos Torres-Verdín[1]

[1]The University of Texas at Austin, Hildebrand Department of Petroleum and Geosystems Engineering, Austin, TX, USA.
[2]Peking University, Department of Energy and Resources Engineering, Beijing, China.
[3]ConocoPhillips Company, Houston, TX, USA.

[*]Corresponding author: Ayaz Mehmani (mehmani.ayaz@utexas.edu)

Abstract

Microfractures originate in hydrocarbon reservoirs and groundwater aquifers either in the form of pore-scale authigenic apertures or secondary openings during well stimulation. Microfractures are often difficult to detect and can act as an invisible impediment when predicting hydrocarbon recovery. We use microfluidics to identify the flow conditions at which microfracture connectivity with macrofractures becomes impactful. The analysis focuses on fluid displacements at unfavorable mobility ratios, which are difficult to capture with high-order numerical methods. Two configurations of microfracture type with the porous matrix, either dead-end (only connected to one macrofracture) or connecting two macrofractures, were investigated as case examples for both water and oil-wet conditions. Our findings confirm that improvements in hydrocarbon recovery are not universal due to the presence of microfractures but rather are a function of capillary number, wettability, and microfracture connectivity. We find that, regardless of wettability, a capillary number threshold for a connected microfractured system exists beyond which the effects of microfractures on recovery, fluid dendrite morphology, and oil ganglia number diminish considerably. However, substantial geometry-dependent differences in recovery are observed below this threshold. A connected microfracture generally decreases hydrocarbon recovery and suppresses coalescence of viscous fingering dendrites regardless of wettability. In contrast, a dead-end microfracture causes wettability-dependent effects with (1) minimal impact on hydrocarbon recovery at water-wet conditions, and (2) both decreasing and increasing recovery effects at oil-wet conditions. Furthermore, dead-end microfractures become somewhat impactful to the divergence of viscous dendrites when capillary number increases but are overall ineffective to the trapped ganglia numbers.

This article has been accepted for publication and undergone full peer review but has not been through the copyediting, typesetting, pagination and proofreading process which may lead to differences between this version and the Version of Record. Please cite this article as doi: 10.1029/2019WR026944

1 Introduction

Microfractures, which we define as openings with aperture sizes similar to matrix pores, occur in the subsurface due to various chemical and mechanical processes related to weathering, tectonic activity, diagenesis, or reactivation of dormant natural fractures during hydraulic fracturing (Gale et al., 2014; Landry et al., 2014; Marechal and Dewandel, 2004). Their presence between macrofractures (those with apertures orders of magnitude larger than matrix pores) can contribute to overall fracture connectivity which has been identified as having significant impact on subsurface flow (Wilke et al., 1985). However, much uncertainty regarding their *in situ* presence and aperture size exists such that seismic and borehole measurements need to be supplemented with transmitted light and scanning electron microscopy to achieve accurate fracture maps (Andres et al, 2014; Landry et al., 2014). In addition, the extent to which this uncertainty is relevant for oil production and NAPL recovery is not clear because predicting transport phenomena, in particular multiphase flow, in fractured rocks is not well established (Berkowitz, 2002). Predictive and conceptual pictures of fracture connectivity and fluid flow are critical for optimizing production (Odling et al., 1999; Matthai et al., 2004; Faulkner et al., 2009).

Unstable immiscible flow (viscous and capillary fingering) (Saffman and Taylor, 1958; Lenormand et al., 1988), may occur in fractured formations during invasion of a less viscous flow (such as fracture fluid) or when performing waterflooding of a dense non-aqueous phase liquid (DNAPL). Previous work on unstable two-phase flow, however, has generally focused on either the competition between viscous and capillary forces, described by capillary number ($Ca = \mu_i v/\gamma$), or the viscosity ratio between the displacing and displaced fluid, quantified by the viscosity ratio ($M = \mu_i/\mu_d$). Pore-scale geometrical effects, such as fracture connectivity, are typically not included when predicting viscous/capillary fingering behavior. In addition to capillary number and viscosity ratio, wettability effects on fingering patterns were recently investigated as a third dimension for a phase diagram in 2D flow cells (Zhao et al., 2016). The investigated pore-scale geometries have generally been 2D (Lenormand et al., 1988), 2.5D (Christensen et al., 2019), or 3D homogeneous porous matrices (Islam et al., 2014) or a single planar rough fracture (Chen et al., 2017). Whether and to what extent the existence of microfractures, connected or dead-end, can affect unstable flow is not yet well known.

Investigating unstable immiscible flow in fractured rocks through numerical modeling is challenging. Direct numerical simulation methods, such as the lattice Boltzmann method (Tsuji et al., 2016), are promising but can be computationally costly in two-scale systems such as those of fractured rocks. Reduced-order methods, such as the dielectric breakdown model (Doorwar and Mohanty, 2014), rely on *a priori* rules for fluid movement that are derived from experimental observations. Although core-flooding has been used to provide measurements within fractured rocks (Rangel-German et al., 2002; Lu et al., 2014; Mirzaei et al., 2016), visualization of pore-level fluid flow behavior in cores (e.g., computerized topography) is difficult, especially in tight rock samples where pore sizes can be smaller than voxel resolution (Wildenschild and Sheppard, 2013; Akbarabadi et al., 2017; Mehmani et al., 2019b). Given that pore sizes in unconventional formations can fall into the nanometer range, nanofluidics and nanomodels are appealing to mimic tight rocks and probe their flow behavior at the subpore (single pores/channels) and pore scales (ensemble of pores) (He et al., 2014; Kelly et al., 2016; Zhong et al. 2018). However, despite their capacity to provide valuable information about nanoconfinement effects on fluid transport, challenges in nanofluidics fabrication and fluid flow visualization are considerable obstacles (Kelly et al., 2015). Given the complexity of nanoporous systems (which is a result of coupled nanoconfinement and geometrical effects) such as mudrocks, decoupling their pore-space geometrical impacts on fluid transport properties with microfluidics can reduce uncertainties associated with measurements acquired with nanofluidics.

Microfluidic systems have been used to investigate multiphase flow and transport phenomena from sub-pore-scale features to more complex porous media, as extensively discussed in recent review papers by Lifton (2016) and Anbari et al (2018). Their capacity for direct visualization of fluid movement in repeatable and controlled environments has allowed the investigation of fundamental physics concepts with simplified geometries. Microfluidics is also an effective screening tool for petroleum applications (Ma et al., 2012; Xu et al., 2015). However, microfluidics studies generally have focused on geometries containing an intact (not fractured) porous matrix or a porous matrix with a single connected fracture

(Wan et al., 1996; Er et al., 2010; Mejia et al., 2019), where the impact of fracture connectivity on flow was not systematically investigated. The two-dimensionality of micromodels may limit their quantitative discoveries to rocks with uniform geometries in the vertical direction or thin geological layers. However, 2D micromodels can capture qualitative two-phase flow trends associated with 3D porous media (Avraam et al., 1994), providing useful observations on pertinent functional relationships. With regard to unstable flow, microfluidics work has generally been performed for probing fingering dendrites in matrix pores (Aminah Setu et al., 2013; Wang et al., 2013; Xu et al., 2014; Zhao et al., 2016) wherein the concept of coupled impacts of microfractures and an adjacent porous matrix were not investigated.

In this paper, we utilize diagnostic microfluidics to investigate the effects of microfracture/macrofracture connectivity on oil recovery and viscous/capillary fingering patterns. Direct experimental observations of two-phase flow in analogue media can assist in reducing the complexity of microfracture transport into several key independent geometrical and flow property variables. We performed water-flood experiments in three micromodel geometries: one with only a porous matrix, one with a connected microfracture (connecting two adjacent and macrofractures) and one with a semi-connected (dead-end) microfracture (only connected to one macrofracture). **Figure 1a** shows a schematic of a hydraulic fracturing operation where microfractures intersect with macrofractures. **Figure 1b** shows the two cases studied in this paper (i.e., the presence of connected microfractures and dead-end microfractures)**. Figure 1c** describes an analogues framework for formulating immiscible flow in a fractured vadose system for NAPL remediation (Faybishenko et al., 2000). Both water- and oil-wet conditions were designed and implemented to determine the impact of wettability on recovery and fingering patterns. Capillary numbers ranging from 10^{-7} (capillary forces are comparatively dominant) to 10^{-5} (viscous forces are comparatively dominant) were selected by changing the flow rate of the injection water. **Figure 2** shows a schematic of fluid and geometrical contributors to the flow patterns within the scope of our work. In addition to other extensively investigated parameters (to the left of the chart), we propose that microfracture connectivity (to the right of the chart) can be regarded as an independent variable for both oil recovery and flow patterns.

2 Methods

Three 2.5-dimensional (2.5D) glass micromodels were fabricated using the method developed by Xu et al. (2017), so that pore throats are shallower than pore bodies. In such 2.5D micromodels, important pore-scale flow phenomena such as the continuity of the wetting phase and capillary snap-off of the non-wetting phase can be captured by having pore-scale 3D features in the 2D pore arrays. This 2.5D feature is important for studying the unstable immiscible flow, where finger initiation has been shown to be sensitive to pore-scale geometries (Chen and Wilkinson, 1985). The three micromodels used in this work are denoted as M1, M2 and M3, with all having a domain size of 2.5 cm in length and 1.5 cm in width and the same porous matrix. M1 is only a homogenous matrix between the inlet and the outlet, M2 has a microfracture in the middle of the matrix connecting only to the inlet side, and M3 has a microfracture in the middle of the matrix connecting the inlet to the outlet (which connects the two macrofractures). In the microfractured micromodels, the microfractures are of comparable size to matrix pores (the depths are both ~21 μm). However, there are two key features that distinguish microfractures from matrix pores, therefore affecting the flow significantly. Firstly, microfractures are lacking in frequent diverging-converging structures, therefore posing little capillary barriers during drainage and serves as “highway” for imbibition along the flow path. Meanwhile, matrix pores have frequent diverging-converging structures, posing capillary barriers to fluid invasion. Secondly, matrix pores are approximately isotropic in average, while microfractures are directional. The photomask designs of the flow domain in M1, M2 and M3 are depicted in **Figure 3a**, where the boundary conditions are also specified. The inlet, outlet and flow channels to/from the flow domain **Figure 3b**. Micromodels are made of soda-lime glass. The grains are cylinders with a near-square cross-section as seen from **Figure 3c**, and the surfaces are macroscopically smooth. The pore-scale geometric features are illustrated in two schematic sketches of the vertical cross-section from two angle (45° and 90° from horizontal direction) as shown in **Figure 3d** and **Figure 3e**. Details regarding the fabrication and micromodel

properties can also be found in the paper by Xu et al (2017). Other relevant geometric properties of the three micromodels are summarized in **Table 1**.

Mineral oil and a crude oil (undisclosed composition) were used as the displaced fluids with viscosities of 170 cp and 230 cp, respectively. The viscosities of water and both oils were measured using Rheometer DHR3 from TA Instrument at 20°C, in the range of 0.1 – 100 s^{-1} which covers the shear rate range in the experiment. The viscosities of both oils stayed constant within the measurement range, confirming that both oils can be approximated as Newtonian fluids in the experiments. The displacing fluid is deionized (DI) water with a viscosity of 1 cp. Viscosity ratios of the displacing fluid (DI water) and the two displaced fluids (mineral oil and crude oil) are 5.8×10^{-3} and 4.3×10^{-3}, respectively. **Table 2** lists the properties of fluids used in this work including their density, viscosity and interfacial tensions. The density of water was computed from the weight of water measured with a digital balance (Adam Equipment HCB123 Highland Digital Precision Balance, with a precision of 0.001g). We measured the weight of 1 ml – 5 ml (1 ml interval) of water and calculated the density from the weight – volume slope. The equipment used for interfacial tension measurement is a spinning drop tensiometer (KRÜSS SDT). The crude oil was pre-equilibrated with deionized water before IFT measurements. We added equal volume of crude oil and deionized water in the same tube and agitated the mixture in an ultrasonic equipment (Branson 2800) for 50 mins when the two fluids were completely mixed. After one week of resting at ambient conditions, oil and water separated into two layers with oil staying on the top layer. 70 and 27 measurements were conducted at 20°C for crude oil – water IFT and mineral oil – water IFT, respectively. The average viscosity values along with the standard deviations were reported in Table 2. While having similar viscosity ratios, the two oils give rise to different wetting states with the glass surface. From the microscopic images shown in **Figure 4**, it is clear that the mineral oil-water-glass system is water-wet, while the crude oil-water-glass system is oil wet. The crude oil-wet state was achieved by aging the micromodel for 24 hours prior to flow experiments. Surface reactions that cause the glass surfaces oil-wetting, such as the adsorption of polar components on the surface, were previously reported in literature (Du et al., 2019).

A total of 18 experiments were performed with the three micromodels (M1, M2 and M3) by systematically varying the capillary number from 10^{-7} to 10^{-5} at two different wettability states (water-wet and oil-wet). To ensure the desired wettability for each experiment, we designed the experiment sequence so that we conducted mineral oil experiments in 3 new micromodels before crude oil experiments, therefore the wettability can be confirmed to be water-wet in 3 mineral oil experiments. The capillary number, *Ca*, was varied by changing the water flow rate from 4 µl/hour to 400 µl/hour, and is given by

$$Ca = \frac{Q_w \mu_w}{WD\gamma} \qquad \text{Equation 1}$$

where Q_w is the injection rate, μ_w is water viscosity, W and D are the width and the etching depth of the micromodel, respectively, and γ is the water-oil interfacial tension. **Table 3** summarizes the capillary number and other properties for each of the 18 experiments. **Figure 5** shows an overlay of experiments conducted in this work in the context of a capillary number-viscosity ratio phase diagram. The viscosity ratio of our experiments is on the order of 5×10^{-3}, and the capillary number is between 10^{-7} and 10^{-4}. We note that according to two phase boundaries determined in the literature (Lenormand et al., 1988; Zhang et al., 2011), our experiments fall approximately into the capillary fingering to viscous fingering cross-over and viscous fingering regions. As is observed subsequently in **Section 3.1.1.**, the dendrite propagations demonstrate characteristic viscous fingering behaviors by moving forward and not forming loops (Lenormand et al., 1988; Zhang et al., 2011). We classify each drainage and imbibition data point into low (~10^{-7}), medium (~10^{-6}) and high (~10^{-5}) capillary number experiments.

For each experiment, the micromodels were saturated with mineral oil or crude oil and aged for 24 hours for crude oil. The aging time needed to create an oil-wet condition is dependent on the type of the system as reviewed by Bartels et al., 2017. In previous microfluidic experiments, many different aging times, from days to weeks, were used to create an oil-wet condition (Song and Kovscek, 2015; Bartels et al., 2017; Du et al., 2019). For our system, we did not have connate water in the glass micromodels before oil invasion, therefore the aging time was shorter as oil contacted the surface the moment it was injected in the micromodels. To expel air from the systems, we injected the oils at a high injection rate using a syringe pump (PHD 2000, Harvard Apparatus) for tens of pore volumes. After saturating micromodels with crude oil, we kept injecting crude oil at a flow rate of 1-2 µl/h during the ageing process. Each of the micromodels was reused in 3 mineral oil and 3 crude oil experiments in order, to eliminate the effects due to even small fabrication difference when using different micromodels. Between experiments, we cleaned the micromodels by injecting hexane, acetone and DI water in sequence. Both organic and inorganic components can be efficiently removed from the system with this cleaning procedure. After cleaning, the micromodels were placed on a hot plate at 110°C for drying. Micromodels were checked under the microscope (Olympus IX73) before each experiment to confirm cleanliness. During the water injection, the micromodels were placed horizontally on top of a light pad. A digital camera (Nikon D5500) was mounted on top of the micromodel to capture time-lapse images. Auto-exposure mode of the camera was enabled to ensure optimal imaging quality according to the background light intensity. Exposure time varied slightly among experiments in the range of 1/160 – 1/250 s. The image resolution is 300 × 300 dpi, and the image dimension is 6000 × 4000 pixels. Time intervals for the injection with low, medium, and high capillary number are 6 mins, 1 min 12 seconds, and 9 seconds, respectively. **Figure 6** shows the experimental system. Immediately after flow experiments, we checked the wettability under the microscope and documented the wettability. We have included pore-scale images captured immediately after flow experiments in *Supporting Information* Section S3. Pore-Scale Visualizations.

Figure 7 demonstrates the image processing procedures we used in this work. Image stacks were cropped to the porous medium domain (2.5 cm × 1.5 cm - see **Figure 3a**) using ImageJ, which is an open-source image processing software (Cates et al., 2004). A set of images captured during each experiment were imported into ImageJ as an image stack. Each image was aligned to the same position using a function called "Linear Stack Alignment" (image registration). Subsequently, the images were cropped around the porous medium regions. The local contrast in each image was enhanced using the "Enhanced Local Contrast (CLAHE)" function. This step ensures that phase boundaries in the images are clear. The images were then binarized using the thresholding method "Otsu" and in order to offset ambient light oscillations, thresholds for each image were set independently from others in the image stack. During color segmentation, the image stack was binarized into black (oil phase) and white (water and grains) for oil recovery curves and number of isolated oil ganglia (see **Figure 7a**). The area fraction of the black (oil) area (within both matrix pores and fractures) in each image was then measured. Oil saturation in each image was calculated as the area fraction in each image divided by the area fraction in the fully oil-saturated image (captured at 0 pore volume). The grey scale distribution (measured using ImageJ's "histogram" function) of the raw and binarized image from a mineral oil experiment and a crude oil experiment (both conducted in M1 at *low* capillary number) are shown in **Figure 7b**. Number of ganglia were determined via a Forest Fire Algorithm (Mehmani et al., 2019a) in which each oil pixel is designated as "unburned" initially. A "fire" is set at each pixel which "burns" all the neighboring pixels until an oil/water interface is reached and isolated oil ganglia are identified. We find that images reveal whether pendular rings between grains can form and are sensitive enough to determine their contribution to fluid film connectivity. However, the non-binary phase distributions within a single pore (which in our results is only the case at high capillary numbers in an unfractured medium) are not captured. We therefore consider the images in meso/Darcy-scale (in contrast to the pore scale where a non-binary phase distribution within a single pore can be captured). For fractal dimension calculation, we focused on the morphology of the invading phase in the mesoscale as well. For this purpose, any influence of grains on fractal dimension values was removed by conducting erosion and dilation procedures on the binarized image (see similar examples by Islam et al (2014), Ferer et al. (2014), and Chen et al. (2017)).

Voxel resolution in our experiments is approximately 12 micrometers/pixel. Sub-resolution features, in particular film thickness and roughness size, are therefore not captured in our analysis. However, they can potentially impact fractal dimension and oil ganglia numbers/sizes if the image resolution were higher. Presence of film in the invaded zones can potentially reduce fractal dimension and increase the number of oil ganglia by fragmenting the invading phase at the subpore-scale (Mehmani et al. 2019a). In addition, when surface roughness is considerable, a two-dimensional quantification of the pore space for fractal analysis is potentially inadequate as the surface roughness generates subpore-scale dynamics, such as pinning and corner flow, which may not be captured at plan-view images such as our experiments. We selected smooth micromodels for our experiments that have surface roughness to pore depth ratios of less than 1%, which according to Mehmani et al. 2019c, subpore-scale dynamics are not enhanced in such surface conditions. Nevertheless, a thorough investigation of sub-resolution impacts is merited as future work. The fractal and ganglia analysis in our work therefore is restricted to the image resolution of experiments.

3 Results and Discussions

3.1 Sweep patterns

3.1.1. Qualitative observations

Experiments show that microfracture connectivity can significantly alter upscaled fingering morphology. In this article, we refer to "upscale" as the scale at which flow behavior is captured with the digital camera throughout the micromodel. **Figure 8a-b** shows the sweep patterns for both imbibition and drainage at breakthrough and steady state**. Figure 8c** summarizes our observations in a conceptual picture for fluid-fluid displacement under unfavorable viscosity ratio in the presence of microfractures (discussed below).

Base case (M1): In the absence of microfractures, fingering is generated only from the macrofracture, as shown in **Figure 8a-b**. We refer to this finger type as macrofracture dendrite (**Figure 8c**). At the time of breakthrough, the initial macrofracture dendrites have penetrated from one macrofracture (inlet side) to the other (outlet side). Macrofractures are not shown **in Figure 8**. Dendrites become narrower as capillary number increases. At steady state, as capillary number increases (regardless of wettability) macrofracture dendrites become narrower but dispersed, which is consistent with observations made by Doorwar and Mohanty (2017). However, the divergence of macrofracture dendrites increases considerably at *high* capillary numbers in water-wet systems, while in oil-wet systems macrofracture dendrites become considerably dispersed starting from *medium* capillary numbers. Macrofracture dendrites are chaotic and do not indicate preferential displacement pathways regardless of capillary number and wettability condition.

Dead-end microfracture (M2): A porous system with a dead-end (semi-connected) microfracture, demonstrates a fingering morphology that is qualitatively distinct from that of an unfractured system (M1), as shown in **Figure 8a-b**. Unlike an unfractured system, fingering dendrites do not exhibit a chaotic movement, but a preferential one determined by the dead-end microfracture. In a dead-end microfractured system, fingering dendrites originate from the dead-end microfracture and are referred to as main microfracture dendrites in **Figure 8c**. At breakthrough, the single main microfracture dendrite has penetrated along the dead-end microfracture while several secondary microfracture dendrites invade the porous matrices. The dendrite patterns are qualitatively similar at *low* to *high* capillary numbers for both imbibition and drainage, while secondary microfracture dendrites become narrower as the capillary number increases. At steady state, macrofracture dendrites only emerge at high capillary numbers but are less dominant than secondary microfracture dendrites. Once the secondary microfracture dendrites develop from the microfracture, they do not traverse backward, causing poor sweep near the upstream end (near the inlet macrofracture). At the tip of the dead-end microfracture, dendrites coalesce more readily and result in a higher sweep compared to the matrix

adjacent to the microfracture. Dendrite patterns are qualitatively similar for both imbibition and drainage, highlighting the dominant role played by the dead-end microfracture compared to wettability.

Microfracture connecting macrofractures (M3): A connected microfractured system demonstrates a distinctly different unstable flow pattern than unfractured (M1) or dead-end microfractured (M2) systems. At *low* to *medium* capillary numbers, the displacing phase traverses mainly through the microfracture and is referred to as main microfracture dendrite in **Figure 8c**. At breakthrough, a main microfracture dendrite prevents the invading phase from entering the matrix which suppresses oil recovery at all capillary numbers. The suppression of fingering is stronger for drainage than imbibition, as a small amount of secondary microfracture dendrites develop during imbibition and in particular at *low* capillary numbers. After breakthrough, when the capillary number reaches a threshold value (between 10^{-5} and 10^{-4}), macrofracture and microfracture dendrites begin to form, which results in an increase in oil recovery, as observed in the steady state images in **Figure 8a-b**. Although additional data points are required to determine the exact threshold capillary number, our results indicate that the threshold is between the viscous fingering and transient regions, as shown in **Figure 5**. The capillary number threshold is furthermore likely to depend on the flow capacity contrast (e.g., permeability contrast) between the microfracture and matrix for which additional experiments are needed. Interestingly, a capillary number threshold for fingering dendrite development is not observed for a dead-end microfractured system (M2). Invasion of secondary microfracture dendrites is more prominent for imbibition at *low* to *medium* capillary number, while the generation of macrofracture dendrites widens for drainage at *high* capillary number.

3.1.2. Quantitative analysis

Fractal dimension (D_f) is used to describe and quantify two-phase flow sweep patterns into capillary fingering or viscous fingering regimes (Lenormand and Zarcone, 1984, 1988; Zhang et al., 2011; Islam et al., 2014; Chen et al., 2017). The fractal dimension varies from 1 to 2, with higher values indicating a coalescent dendrite evolution. Quantifying sweep patterns can have other applications as well, such as determining functional relationships for a chemical's dissipation rate at the evolving immiscible interface. We therefore utilize fractal dimension to investigate the impact of dead-end and connected microfractures on unstable flow morphology. **Figure 9a**, adapted from Chen et al. (2017), compares the visual morphology of fingering patterns and fractal dimension. The fractal dimension of an immiscible front has generally been investigated as a function of capillary number and viscosity ratio, while (as discussed in the Introduction) geological effects such as connectivity of microfractures, are typically not considered when studying their variability. For the computation details of the fractal dimensions, an example of the box-counting method is described in the *Supporting Information* Section S1. Fractal Dimension Analysis.

Figure 9b shows the fractal dimension of the micromodels at steady state. We observe that the lowest fractal dimension belongs to the connected microfractured system at oil-wet conditions and *low* capillary numbers. As is revealed in **Figure 8**, a connected microfractured system predominantly displays a main microfracture dendrite pattern prior to reaching a capillary number threshold. We also observe that changing the wettability from oil wet to water wet slightly increases the fractal dimension. This behavior is partly due to the presence of secondary microfracture dendrites which give rise to a more coalescent fingering pattern. At *low* capillary number and regardless of wettability, a dead-end microfracture reduces the front fractal dimension as well, even though its impact is less than due to a connected microfracture. The effects of a dead-end microfracture on fractal dimension are consistent with our observation in **Figure 8a-b**; the microfracture decreases the chaotic movements of the dendrites by providing a preferential pathway in the middle of the porous domain. Similar to a connected microfractured system, the main microfracture dendrite traverses through the microfracture itself and effectively develops a Saffman finger with low dendrite divergence. At *medium* capillary numbers, the impact of a connected microfracture is similar to low capillary numbers in reducing the front fractal dimension. However, the ability of a dead-end microfracture to confine dendrite divergence decreases at *medium* capillary numbers while secondary microfracture dendrites increase the fractal dimension compared to the unfractured system. At *high* capillary numbers, differences between fractal dimension for the three micromodel types and two wettability conditions decrease considerably. This reduction is

due to the inefficacy of microfractures, dead-end or connected, from influencing the sweep patterns of the invading phase beyond a capillary number threshold.

Figure 9c, illustrates the fractal dimension of the dendrites throughout the evolution of the invading front. We notice that as capillary trapped oil saturation decreases, fractal dimension generally increases. This increase is due to the evolution of fingering dendrites as they become more likely to coalescence and decrease the capillary trapped oil saturation. However, at equal oil recovery values, only a connected microfracture (M3) at *high* capillary numbers (regardless of wettability) suppresses the divergence of fingering dendrites. This contrast in microfracture connectivity effects with the steady-state values shown in **Figure 9b** highlights the importance of capillary trapped saturation in properly assessing dendrite morphology. In other words, if a recovery operation is conducted at *low* and *medium* capillary numbers, the recovered oil saturation is sufficient information for monitoring its performance, while connectivity effects of microfractures on sweep patterns become negligible. This assumption is valid for both water- and oil-wet systems but becomes invalid at high capillary numbers where microfracture connectivity is a relevant parameter in determining flow patterns when monitoring recovery.

3.2 Oil recovery

Figure 10 shows the oil saturation versus pore volumes injected for each microfractured system at three capillary numbers and both wettability conditions. **Figure 11** shows functional relationships for ultimate oil recovery and pore volumes required to reach steady state as functions of capillary number. The recovery and pore volume values shown in **Figures 10-11** are also summarized in **Tables 4 and 5.**

Base case (M1): The analysis in **Figures 10** and **11a** shows that recovery slightly increases with capillary number by up to 5% in water-wet systems, where fingers become more dispersed and sweep larger areas. During drainage**,** however, recovery at *medium* capillary number is the lowest while recovery at *high* capillary number is highest. The largest recovery difference is 18%. As shown qualitatively in **Figure 8**, fingers become more dispersed but narrower with the increase in capillary number. The two effects compete with each other, resulting in a non-monotonic trend in recovery versus capillary number.

Dead-end microfracture (M2): Dead-end microfractures in water-wet systems, despite changes in dendrite generation mechanism, do not alter ultimate recovery significantly regardless of capillary number (see **Figures 10** and **11a).** In fact, recovery differences due to presence of a dead-end microfracture are less than 5%. In oil-wet dead-end microfractured systems, recovery discrepancies can increase up to 17% but unlike water-wet systems, oil recovery can both increase or decrease depending on the capillary number. This higher dependence on capillary number for drainage can be due to the dominance of pore-scale bulk velocities (in contrast to the presence of corner films for imbibition) on immiscible flow (Zhao et al., 2016). However, additional numerical simulations (Alpak et al., 2018) or particle image velocimetry experiments (Kazemifar et al., 2015) are needed to determine the precise impact of wettability on capillary number dependence for oil recovery. **Figure 11b** and **Table 5** show that dead-end microfractures, at almost all capillary numbers, delay oil recovery by increasing the amount of injected pore volumes required to reach 95% recovery. This delay is most significant in oil-wet systems and *high* capillary numbers. In an unfractured system (M1), oil recovery reaches steady state rapidly once preferential pathways are established at the early stages of injection and leave oil ganglia trapped in the remaining regions. By contrast, in a dead-end microfractured system after the early stage pathways are formed, water continues to sweep into the remaining regions, resulting in long tails of up to tens of pore volumes in the recovery curves shown in **Figure 10.**

Microfracture connecting macrofractures (M3): As shown in **Figures 10-11**, prior to reaching a capillary number threshold, a connected microfracture decreases oil recovery significantly**.** The decrease in recovery is more prominent in oil-wet systems because water can enter the matrix from the microfracture during imbibition (secondary microfracture dendrites as shown in **Figure 8c**). However, at *high* capillary numbers, ultimate recovery in a connected microfractured system is similar to (1% lower in in water-wet systems) or higher (12% in oil-wet systems) than for an unfractured system. The

increase of oil recovery could indicate that the pressure difference from upstream to downstream in porous matrices in the connected microfracture system overcomes the largest capillary pressure pinning the oil between two macrofractures. As observed in Figure 11b, similar to a dead-end microfracture, a connected microfracture can delay oil recovery but only beyond a capillary number threshold (i.e. *high* capillary numbers). The long tail in capillary trapped saturation curves indicates that water continues to sweep into the matrix after breakthrough along the microfracture. The tail lengths for M3 are comparable to those of M2 because the pore volumes injected at 95% oil recovery are similar. From **Figure 11a**, we find that an increase of capillary number improves oil recovery for unfractured and dead-end microfractured systems regardless of wettability. In a connected microfractured system, however, oil recovery can significantly improve (up to 56% in drainage and up to 24% in imbibition) at *high* capillary numbers, especially during drainage. From observing the immiscible phase distributions in **Figure 8**, we interpret that the connected microfracture establishes hydraulic connectivity for the invading phase between the two macrofractures at breakthrough. Given (1) the narrow cross-section of the microfracture compared to the domain cross-section, and (2) the constant flow rate condition, the pressure difference for the invading phase between the two macrofractures becomes highest compared to those of the dead-end and matrix systems. The heightened pressure difference gives rise to a higher imposed "global" capillary pressure which drives the oil-in place considerably to the outlet.

As discussed by Tanino and Christensen (2019), capillary end effects can become considerable for water invasion in oil-wet media that are conducted in micromodels with domain sizes similar to this work. Our predictions of oil recovery with those cases are therefore smaller than what would be expected if capillary end effects did not exist. However, in fractured tight reservoirs, capillary end effect can be naturally present due to extreme small matrix pore sizes (2 – 3 orders of magnitude smaller than in micromodels) and frequent microfractures, where the increased capillary end effective length would become comparable to fracture spacing. Our designs can therefore serve as analogues for investigating recovery in the presence of naturally occurring capillary end effects in the subsurface, where the results are quantitatively significant. In addition, our aim is to capture the invasion patterns qualitatively and parameterize them quantitatively, even though the precise values presented in this work may not translate to subsurface conditions. In qualitative aspect, as presented in **Figures 8ab** the invasion patterns are mostly determined at an early stage prior to breakthrough conditions when end effects are not yet effective (that is the invading phase has not yet sensed the domain end). Finally, given that similar domain sizes were used in this work, conclusions based on comparing flow patterns at various capillary numbers for each wettability condition, even though capillary end effects are potentially present, are still valuable for our understanding of microfracture effects during unstable flow.

We aimed to provide a straight-forward, semi-quantitative comprehension of the interplay between the microfractures and the porous matrix and their effects on unstable two-phase flow. A comprehensive reproducibility study is not within the scope of this work, but from several replicate experiments performed in the 3 micromodels, the trend of the water invasion patterns in all three geometries are qualitatively reproducible. Quantitatively, we were also able to obtain good reproducibility as the remaining saturations are comparable with 5% variations in recovery which agrees with the literature on the reproducibility of micromodels' study on unstable two-phase flow (Ferrari et al., 2015). All replicated experiments are included in *Supporting Information* S2. Reproducibility Study."

3.3 Oil ganglia analysis

3.3.1 Ganglia distribution post water-flooding

Figure 12 depicts the distribution of oil ganglion size at steady state for our experiments. We define oil ganglion size as the actual size of each ganglion divided by the size of one pore. Ganglion sizes are divided into 10 size groups with the calculated areal percentage of remaining oil for each group.

Base case (M1): In both imbibition and drainage processes, oil ganglion size decreases with an increase in capillary number as the plot shifts to the right (smaller size groups). During imbibition, oil ganglia

larger than 500 take 62% of the total remaining oil at *low* capillary numbers and decrease to 46% at *medium* capillary numbers and 0% at *high* capillary numbers. During drainage, the percentage of oil ganglia larger than 500 decreases from 42% to 19% and 0% as the capillary number increases. This discrepancy due to wettability alteration agrees with the qualitative observation made from **Figures 8** that the fingers are narrower under oil-wet conditions, resulting in overall smaller ganglion sizes.

As was shown in **Figure 11a**, oil recovery increases with capillary number, therefore smaller oil ganglia correspond to higher recovery factors. However, the increase in oil recovery is less significant than the decrease in oil ganglion size because the increase of oil recovery is only 5-15% under both wetting conditions. As shown in **Figure 12**, although the percentage of the biggest oil ganglia decreases, the distribution tail containing smaller oil ganglia widens. For a given capillary trapped saturation, smaller oil ganglia can result in a higher spread of the injected phase, which is advantageous in chemical treatments. However, we observe that smaller remaining oil ganglia at the earlier stages are more difficult to recover compared to larger ones during continuous water flooding.

Dead-end microfracture (M2): In a dead-end microfractured system, oil ganglion sizes decrease with capillary number but not as considerably as in an unfractured system. The decrease in the percentage of the largest oil ganglion group (>500) is 27% and 29% for imbibition and drainage processes which is much lower than the 62% and 42% decrease observed in an unfractured system. In contrast to M1, oil ganglia in the porous matrix in M2 are more difficult to mobilize even at *high* capillary numbers, as shown in **Figure 8.** Number of fingers that are generated in the porous matrix from the inlet (macrofracture) and microfracture increases with capillary number. The finger generation phenomenon decreases the size of large oil ganglia (>500) and contributes to the increase in oil recovery. Compared to M1, we found that the fragmentation of the large ganglion may not be efficient for improving recovery because smaller oil ganglia are harder to mobilize than larger ones at later stages.

Microfracture connecting macrofractures (M3): Recovery from the porous matrix is low at *low* to *medium* capillary numbers, leaving large oil ganglia (occupying >1000 pores) trapped in the porous matrix. **Figure 12** shows that approximately 99% of the remaining oil is in the largest size group (>500 pores). At *high* capillary numbers ~10^{-5}, the oil ganglion size decreases significantly compared to unfractured and dead-end microfractured systems. In a connected microfractured system, the largest oil ganglia is 100 to 500 times the pore volume when water wet and 10 to 25 times the pore volume when oil wet. This sharp decrease of oil ganglion size in the porous matrix is consistent with the significant increase of oil recovery observed at *high* capillary numbers. At *low* to *medium* capillary numbers, water flows primarily through the microfracture, leaving large oil ganglia trapped in the matrix. At *high* capillary numbers, however, water dendrites enter into the matrix from the macrofracture and shrink the oil ganglia into smaller and more scattered oil ganglia. The fragmentation of the large oil ganglia contributes to the significant increase of oil recovery as capillary number increases.

3.3.2 Ganglia generation during displacement processes

Figure 13a shows the number of generated oil ganglia as a function of capillary trapped oil saturation. We notice that the presence of a connected microfracture suppresses oil ganglia generation significantly. This reduction in oil ganglia number is for all capillary numbers and wettability conditions as long as fingering dendrites other than the main dendrite type shown in **Figure 8c** is generated. Flow patterns shown in **Figure 8a-b** verify that a connected microfracture can act as a point of convergence for fingering dendrites such that they are precluded from entering the matrix. In addition, given its higher hydraulic conductivity, a connected microfracture decreases the local velocity of the invading phase inside the matrix. A reduction in local velocity can enhance the coalescence of fingering dendrites. In contrast to a connected microfracture, a dead-end microfracture does not suppress oil ganglia generation significantly. This difference in oil ganglia generation is due to the ability of the invading dendrites to enter the matrix from the microfracture. Such a behavior results in front divergence similar to that of an unfractured system. As discussed in *subsection 3.1.2.*, capillary trapped oil saturation may not be sufficient information for monitoring an enhanced oil recovery operation because it does not capture the spatial distributions of two immiscible phases. In **Figure 13a** we observe that capillary trapped oil saturation alone cannot predict the total number of oil ganglia at a particular oil recovery step. Whether a microfracture is present and is connecting two macrofractures needs to be determined when predicting

oil ganglia generation. Information about oil ganglia number can in fact become critical information during the development of a tertiary recovery operation. **Figures 13b-c** show aggregate depictions of all the data into a single plot for both imbibition and drainage. The plots clarify that the highest number of ganglia form in the absence of microfractures and at *high* capillary numbers. Furthermore, we find that variations between each ganglia generation plots are more prominent during drainage than imbibition. The increase in variation indicates a higher sensitivity to capillary number for oil ganglia generation in oil-wet systems. This difference is likely due to the absence of corner film percolation during drainage, which results in the bulk flow within channels becoming the main displacing mechanism. The higher sensitivity to capillary numbers at oil-wet conditions is consistent with measurements made in micromodels for immiscible displacement with varying wettability (Zhao et al., 2016).

3.4 Implications and limitations

Fractures are ubiquitous in subsurface systems, potentially influencing the outcome of many hydrocarbon recovery and environmental remediation projects. Although fractures are recognized to affect transport phenomena, quantifying the various uncertainties about their impact on two-phase immiscible flow is still an important and open research topic. This is largely due to the technical challenge of quantifying fluid transport in fractured systems which takes place through multiple length scales. The need for experimental data that visualize fluid transport in fractured rocks is also necessary to verify multiscale numerical models. However, the majority of experimental research has currently focused on single fractures to understand the impact of fracture surface rugosity and aperture distribution. Our work provides direct observations of fluid transport in macrofracture/microfracture ensembles. These observations can guide the development and verification of numerical algorithms for immiscible fluid dynamics with near-wellbore reservoir simulators for hydraulically fractured formations (Wang and Leung, 2015) and remediation projects in the vadose zone (Faybishenko et al., 2000). For instance, our results indicate using geological markers to determine if natural fracture presence or healing is relevant only below a critical capillary number threshold. Furthermore, we find that formation wettability is an irrelevant parameter when determining the implications of natural fracture openness based on geological investigations. Although not pursued in this article, a hybrid numerical-experimental approach based on our framework can be a next step in investigating transport properties of fractured rocks during unstable flow. This approach would follow the approach by Li et al. (2020) and Berg et al. (2016) and can potentially determine several key functional relationships such as that between relative permeability (k_{rw}) and water saturation (S_w). A hybrid numerical-experimental approach can furthermore be used to assess the viability of cost-effective computational fluid dynamics within a broad capillary number/wettability parameter space.

While capturing the essential features of fracture rock systems, our experimental models have certain simplifications, especially concerning geometrical design. More specifically:

- The porous matrices in the three micromodels are artificially designed as homogeneous pore arrays. Such homogeneity, when coupled with fractures, may affect the flow behavior. This limitation could be improved by replicating the patterns observed in thin sections of fractured rocks.

- Although the 2.5D pore models have pore-scale 3D features by having pore-to-pore connections in the third dimension, they are still insufficient to quantify the effects of connectivity in true 3D space. However, two-dimensional micromodels are still capable of serving as diagnostic tools for identifying multiphase flow dynamics phenomena and providing conceptual pictures of them (Avraam et al., 1994; Armstrong and Berg, 2013). The qualitative findings of our work, such as the viscous fingering generation mechanisms shown in **Figure 8c** are likely applicable for three-dimensional fractured formations. In contrast, our quantitative observations (and microfluidics research in general), are more useful for concluding trends and providing first order approximations for characterizing two-phase flow dynamics. A review of

utility of microfluidics (and nanofluidics) in improving predictions of subsurface operations are provided in Mehmani et al. (2019d).

- Measurements are all acquired at the inch-long scale restricted by the size of the models. Upscaling by experimental or numerical methods is needed before applying our results to the spatial scales of actual subsurface operations.

- The microfracture-porous matrix system is simplified because the fractures are designed to be straight and symmetric through the porous matrices, constant in depth, and to exhibit rectangular cross-sections. Such basic designs could be modified for examining different rock conditions and consequences on multi-phase fluid flow.

- This work explores phenomena at various macroscopic capillary numbers which is linked to the competition between the length scale of the capillary dispersion zone and the length scale of the observed domain (Berg and Ott, 2012; Armstrong et al., 2014) while the viscosity ratio was kept constant. It is also of great interest to systematically change the viscosity ratio and study the corresponding effects on fluid flow for various fracture rock systems. Future work may consider a wider capillary number, viscosity ratio, and wettability parameter space to provide insight into the validity of both macroscopic and microscopic dimensionless parameters in fractured systems. The onset of front instability and capillary desaturation (which has been computed for homogenous rocks by Oughanem et al. (2015) and Hilfer et al. (2015)) can be determined thereafter when channeling due to microfractures is present. Whether the presence of microfractures is of great influence in the competition of the two length scales (capillary and viscous length scales), and whether microfractures introduce a critical third length scale, remain in question and require additional work.

- Micromodels were chosen instead of nanomodels due to their low cost, tractable fabrication steps, and strong visualization ability to complete the systematic experimental research effort described in this paper (18 flooding experiments in total). Results obtained from our investigation are therefore suitable for formations with micrometer-scale pores (such as aquifers and certain multiscale tight formations). However, our results can be extended to nanoporous systems such as mudrocks, in order to decouple the impact of pore topology from nanoconfinement effects on fluid phase distributions and oil/NAPL recovery.

4. Conclusions

While relatively large conduits such as fractures enhance single-phase flow in rocks, the impact of their properties on multi-phase flow (a more common subsurface condition) remains unclear. Controlled microfluidic experiments yielded the following insights concerning the combined effect of microfracture connectivity, wettability, and capillary number on oil recovery:

- Three distinct viscous fingering generation mechanisms in the presence of microfractures were identified. The dominance of each mechanism depends on both microfracture connectivity and capillary number. Wettability does not affect the conceptual pictures for the generation of fingering dendrites.
- Each dendrite generation mechanism affects front morphology, oil ganglia number, and, ultimately, oil recovery depending on capillary number and wettability conditions.
- A connected microfracture has the most influence in (1) suppressing oil recovery, (2) dendrite coalescence, and (3) oil ganglia generation. However, this influence decreases beyond a threshold capillary number between 10^{-5} and 10^{-4}.
- Despite confirming a unique dendrite generation mechanism, dead-end microfractures have only minor impact on oil recovery under water-wet conditions.

Overall, our experimental observations (1) challenge the single-phase conceptual picture that microfracture connectivity necessarily improves recovery, and (2) highlight the complexity of multi-phase transport within microfractures. The systematic experimental data presented in this paper provide

benchmarking opportunities for mechanistic models and shed valuable insight for the development of reliable conceptual pictures of two-phase flow in spatially complex fractured rocks.

Acknowledgements

Use of The University of Texas at Austin's Center for Nano and Molecular Science cleanroom was vital to this work and we thank the Welch Foundation for supporting those facilities. We would like to thank the sponsors of the Chemical EOR Industrial Affiliates Research Project at the University of Texas at Austin for their support. This research was furthermore supported by the University of Texas at Austin's Research Consortium on Formation Evaluation, sponsored by Anadarko, Aramco, Baker Hughes, BHP Billiton, BP, Chevron, ConocoPhillips, COSL, DEA, ENI, Equinor ASA, Exxonmobil, Halliburton, INPEX, Lundin-Norway, Nexen-CNOOC, Oil Search Alaska, OXY, Petrobras, Repsol, Schlumberger, Shell, Southwestern Energy, TOTAL, Woodside, Wintershall. Carlos Torres-Verdín is thankful for the financial support provided by the Brian James Jennings Memorial Endowed Chair in Petroleum and Geosystems Engineering. **Data generated for this paper can be accessed from Texas Data Repository and will be made public upon acceptance of the paper. Private URLs of each dataset for the reviewers are provided in the supplementary information attachment.**

Nomenclature

NAPL	Non-aqueous phase liquid
Ca	Capillary number
M	Viscosity ratio
S_o	Oil saturation
2D	Two dimensional
2.5D	Two and a half dimensional: throats are shallower than pores in the micromodel
3D	Three dimensional
Q_w	Injection rate ($\mu L/hr$)
μ_w	Water viscosity (cp)
W	Micromodel width (cm)
D	Pore depth (μm)
γ	Interfacial tension (mN/m)
k_{rw}	Water relative permeability
S_w	Water saturation

References

Akbarabadi, M., Saraji, S., Piri, M., Georgi, D. and Delshad, M. 2017. Nano-Scale Experimental Investigation of in-situ Wettability and Spontaneous Imbibition in Ultra-Tight Reservoir Rocks: *Advances in Water Resources* **107**: 160–179. https://doi:10.1016/j.advwatres.2017.06.004

Alpak, F.O., Zacharoudiou, I., Berg, S., Dietderich, J. and Saxena, N. 2018. Direct Simulation of Pore-Scale Two-Phase Visco-Capillary Flow on Large Digital Rock Images using a Phase-Field Lattice Boltzmann Method on General-Purpose Graphics Processing Units. *Computational Geosciences*: 1–32. https://doi.org/10.1007/s10596-019-9818-0

Anbari, A., Chien, H.T., Datta, S.S, Deng, W., Weitz, D.A. and Fan, J. 2018. Microfluidic Model Porous Media: Fabrication and Applications. *Small* **14** (18): 1703575. https://doi.org/10.1002/smll.201703575

Armstrong, R.T. and Berg, S. 2013. Interfacial Velocities and Capillary Pressure Gradients during Haines Jumps. *Physical Review E* **88** (4): 043010. https://doi.org/10.1103/PhysRevE.88.043010

Armstrong, R.T., Georgiadis, A., Ott, H., Klemin, D. and Berg, S. 2014. Critical Capillary Number: Desaturation Studied with Fast X-Ray Computed Microtomography. *Geophysical Research Letters* **41** (1): 55–60. https://doi.org/10.1002/2013GL058075

Avraam, D.G., Kolonis, G.B., Roumeliotis, T.C., Constantinides, G.N. and Payatakes, A.C. 1994. Steady-State Two-Phase Flow through Planar and Nonplanar Model Porous Media. *Transp. Porous Media* **16** (1): 75–101. https://doi.org/10.1007/BF01059777

Bartels, W.-B., Mahani, H., Berg, S. et al. 2017. Oil Configuration under High-Salinity and Low-Salinity Conditions at Pore Scale: A Parametric Investigation by Use of a Single-Channel Micromodel. *SPE Journal* **22** (5): 1362–1373. SPE-181386-PA. https://doi.org/10.2118/181386-PA.

Berg, S. and H. Ott, H. 2012. Stability of CO2–Brine Immiscible Displacement. *International Journal of Greenhouse Gas Control* **11**: 188–203. https://doi.org/10.1016/j.ijggc.

Berg, S., Rücker, M., Ott, H., Georgiadis, A., Van der Linde, H., Enzmann, F., Kersten, M., Armstrong, R.T., De With, S., Becker, J. and Wiegmann, A. 2016. Connected Pathway Relative Permeability from Pore-Scale Imaging of Imbibition. *Advances in Water Resources* **90**: 24-35. https://doi.org/10.1016/j.advwatres.2016.01.010

Berkowitz, B. 2002. Characterizing Flow and Transport in Fractured Geological Media: A Review. *Advances in Water Resources* **25**: 861–884. https://doi.org/10.1016/S0309-1708(02)00042-8

Cates, J.E, Lefohn, A.E. and Whitaker, R.T. 2004, GIST: an Interactive, GPU-Based Level Set Segmentation Tool for 3D Medical Images. *Medical Image Analysis* **8**: 217–231. https://doi.org/doi:10.1016/j.media.2004.06.022

Chen, J.-D. and Wilkinson, D. 1985. Pore-Scale Viscous Fingering in Porous Media. *Phys. Rev. Lett.* **55**: 1892–1895. https://doi.org/10.1103/PhysRevLett.55.1892

Chen, Y.-F., Fang, S., Wu, D.-S. and Hu, R. 2017. Visualizing and Quantifying the Crossover from Capillary Fingering to Viscous Fingering in a Rough Fracture. *Water Resour. Res.* **53**: 7756–7772. https://doi.org/10.1002/2017WR021051

Christensen, M., Zacarias-Hernandez, X. and Yukie Tanino, Y. 2019. Impact of Injection Rate on Transient Oil Recovery under Mixed-Wet Conditions: a Microfluidic Study. *E3S Web of Conferences* **89** 04002. https://doi.org/10.1051/e3sconf/20198904002

Doorwar, S. and Mohanty, K.K. 2017. Viscous-Fingering Function for Unstable Immiscible Flows. *SPE J.* **22** (1): 19–31. SPE-173290-PA. https://doi.org/10.2118/173290-PA

Doorwar, S. and Mohanty, K.K. 2014. Extension of the Dielectric Breakdown Model for Simulation of Viscous Fingering at Finite Viscosity Ratios. *Phys. Rev. E* **90**, 013028. https://doi.org/10.1103/PhysRevE.90.013028

Du, Y., Xu, K., Mejia, L., Zhu, P. and Balhoff, M. 2019. Microfluidic Investigation of Low-Salinity Effects during Oil Recovery: A No-Clay and Time-Dependent Mechanism. *SPE J.* Preprint. SPE-197056-PA. https://doi.org/10.2118/197056-PA

Er, V., Babadagli, T. and Xu, Z. 2010. Pore-Scale Investigation of the Matrix−Fracture Interaction during CO2 Injection in Naturally Fractured Oil Reservoirs. *Energy Fuels* **24** (2): 1421–1430. https://doi.org/10.1021/ef901038v

Faulkner, D.R., Jackson, C.A.L., Lunn, R.J., Schlische, R.W., Shipton, Z.K., Wibberley, C.A.J. and Withjack, M.O. 2009. A Review of Recent Developments Concerning the Structure, Mechanics and Fluid Flow Properties of Fault Zones. *Journal of Structural Geology* **32** (11):1557–1575. https://doi.org/10.1016/j.jsg.2010.06.009

Ferrari, A., Jimenez-Martinez, J., Borgne, T.L., Méheust, Y. and Lunati, I. 2015. Challenges in Modeling Unstable Two-Phase Flow Experiments in Porous Micromodels. *Water Resources Research* **51**: 1381–1400, https://doi.org/10.1002/2014WR016384

Gale, J.F.W., Laubach, S.E., Olson, J.E., Eichhubl, P. and Fall, A. 2014. Natural Fractures in Shale: A Review and New Observations. *AAPG Bull.* **98** (11): 2165–2216. https://doi.org/10.1306/08121413151

Faybishenko, B., Doughty, C., Steiger, M., Long J.C., Wood, T.R., Jacobsen, J.S., Lore, J. and Zawislanski, P.T. 2000. Conceptual Model of the Geometry and Physics of Water Flow in a Fractured Basalt Vadose Zone. *Water Resources Research* **36** (12): 3499–520. https://doi.org/10.1029/2000WR900144

He, K., Xu, L., Gao, Y., Neeves, K.B., Yin, X., Bai, B., Ma, Y. and Smith, J. 2014. Validating Surfactant Performance in the Eagle Ford Shale: A Correlation between the Reservoir-on-a-Chip Approach and Enhanced Well Productivity. Presented at SPE Improved Oil Recovery Symposium, 12-16 April, Tulsa, Oklahoma, USA. SPE-169147-MS. https://doi.org/10.2118/169147-MS

Hilfer, R., Armstrong, R.T., Berg, S., Georgiadis, A. and Ott, H. 2015. Capillary Saturation and Desaturation. *Phys. Rev. E* **92** (6): 063023. https://doi.org/10.1103/PhysRevE.92.063023

Islam, A., Chevalier, S., Ben Salem, I., Bernabe, Y., Juanes, R. and Sassi, M. 2014. Characterization of the Crossover from Capillary Invasion to Viscous Fingering to Fracturing during Drainage in a Vertical 2D porous medium. Int. J. *Multiph. Flow* **58**: 279–291. https://doi.org/10.1016/j.ijmultiphaseflow.2013.10.002

Kazemifar, F., Blois, G., Kyritsis, D.C. and Christensen, K.T. 2015. A Methodology for Velocity Field Measurement in Multiphase High-Pressure Flow of CO2 and Water in Micromodels. *Water Resources Research* **51** (4): 3017–3729. https://doi.org/10.1002/2014WR016787

Kelly, S., Torres-Verdín, C. and Balhoff, M.T. 2015. Quantification of Bulk Solution Limits for Liquid and Interfacial Transport in Nanoconfinements. *Langmuir* **31** (7): 2167–2179. https://doi.org/10.1021/la504742w

Kelly, S., Torres-Verdín, C. and Balhoff, M.T. 2016. Anomalous Liquid Imbibition at the Nanoscale: the Critical Role of Interfacial Deformations. *Nanoscale* **8** (5): 2751–2767. https://doi.org/10.1039/c5nr04462f

Landry, C., Eichhubl, P., Prodanovic, M. and Tokan-Lawal, A. 2014. Matrix-Fracture Connectivity in Eagle Ford Shale. Presented at Unconventional Resources Technology Conference, 25-27 August, Denver, Colorado, USA. https://doi.org/10.15530/URTEC-2014-1922708

Lenormand, R. and Zarcone, C. 1984. Role of Roughness and Edges during Imbibition in Square Capillaries. Presented at SPE Annual Technical Conference and Exhibition, 16-19 September, Houston, Texas. https://doi.org/10.2118/13264-MS

Lenormand, R., Touboul, E. and Zarcone, C. 1988. Numerical Models and Experiments on Immiscible Displacements in Porous Media. *J. Fluid Mech.* **189**: 165–187. https://doi.org/10.1017/S0022112088000953

Li, X., Berg, S., Castellanos-Diaz, O., Wiegmann, A. and Verlaan, M. 2020. Solvent-Dependent Recovery Characteristic and Asphaltene Deposition during Solvent Extraction of Heavy Oil. *Fuel* **263**: 116716. https://doi.org/10.1016/j.fuel.2019.116716

Lifton, V.A. 2016. Microfluidics: an enabling screening technology for enhanced oil recovery (EOR). *Lab on a Chip* **16**: 1777–1796. https://doi.org/10.1039/C6LC00318D

Lu, L., Goudarzi, A., Peila Chen, P., Kim, D.H., Delshad, M., Mohanty, K.K., Sepehrnoori, K., Weerasooriya, U.P. and Pope, G.A. 2014. Enhanced Oil Recovery from High-Temperature, High-Salinity Naturally Fractured Carbonate Reservoirs by Surfactant Flood. *Journal of Petroleum Science and Engineering* **124**: 122–131. https://doi.org/10.1016/j.petrol.2014.10.016

Ma, K., Liontas, R., Conn, C.A., Hirasakia, G.J. and Biswal, S.L. 2012. Visualization of improved sweep with foam in heterogeneous porous media using microfluidics. *Soft Matter* **8** (41): 10669–10675. https://doi.org/10.1039/C2SM25833A

Maréchal, J.C., Dewandel, B. and Subrahmanyam, K. 2011. Use of Hydraulic Tests at Different Scales to Characterize Fracture Network Properties in the Weathered-Fractured Layer of a Hard Rock Aquifer. *Water Resources Research* **40** W11508. https://doi.org/10.1029/2004WR003137

Matthäi, S.K. and Belayneh, M. 2004. Fluid Flow Partitioning between Fractures and a Permeable Rock Matrix. *Geophysical Research Letters* **31** (7): L07602. https://doi.org/10.1029/2003GL019027

Mehmani, A., Kelly, S., Torres-Verdín, C. and Balhoff, M. 2019a. Residual Oil Saturation following Gas Injection in Sandstones: Microfluidic Quantification of the Impact of Pore-Scale Surface Roughness. *Fuel* **251**: 147–161. https://doi.org/10.1016/j.fuel.2019.02.118

Mehmani, A., Kelly, S. and Torres-Verdín, C. 2019b. Leveraging Digital Rock Physics Workflows in Unconventional Petrophysics: A Review of Opportunities, Challenges, and Benchmarking. Presented at SPWLA 60th Annual Logging Symposium, 15-19 June, the Woodlands, Texas, USA. https://doi.org/10.30632/T60ALS-2019_QQ

Mehmani, A., Kelly, S., Torres-Verdín, C, and Balhoff, M. 2019c. Capillary Trapping Following Imbibition in Porous Media: Microfluidic Quantification of the Impact of Pore-Scale Surface Roughness. *Water Resources Research* **55** (11): 9905–9925, https://doi.org/10.1029/2019WR025170

Mehmani, A., Kelly, S. and Torres-Verdín, C. 2019d. Review of Micro/Nanofluidic Insights on Fluid Transport Controls in Tight Rocks. *Petrophysics* **60** (06): 872–90. SPWLA-2019-v60n6a10

Mejia, L., Tagavifar, M., Xu, K., Mejia, M., Du, Y. and Balhoff, M. 2019. Surfactant Flooding in Oil-Wet Micromodels with High Permeability Fractures. *Fuel* **241** (1): 117–1128. https://doi.org/10.1016/j.fuel.2018.12.076

Mirzaei, M., DiCarlo, D.A. and Pope, G.A. 2016. Visualization and Analysis of Surfactant Imbibition into Oil-Wet Fractured Cores. *SPE J.* **21** (01): 101–111. SPE-166129-PA. https://doi-org.ezproxy.lib.utexas.edu/10.2118/166129-PA

Niemeyer, L., Pietronero, L. and Wiesmann, H.J., 1984. Fractal dimension of dielectric breakdown. Physical Review Letters, 52(12), p.1033. https://doi.org/10.1103/PhysRevLett.52.1033

Odling, N.E., Gillespie, P., Bourgine, B., Castaing, C., Chiles, J.P., Christensen, N.P., Fillion, E., Genter, A., Olsen, C., Thrane, L.,Trice, R., Aarseth, E., Walsh J.J. and Watterson, J. 1999. Variations in Fracture System Geometry and Their Implications for Fluid Flow in Fractures Hydrocarbon Reservoirs. *Petroleum Geoscience* **5**: 373-384. https://doi.org/10.1144/petgeo.5.4.373

Oughanem, R., Youssef, S., Bauer, D. et al. 2015. A Multi-Scale Investigation of Pore Structure Impact on the Mobilization of Trapped Oil by Surfactant Injection. *Transp Porous Med* **109**: 673–692. https://doi.org/10.1007/s11242-015-0542-5

Saffman, P.G. and Taylor, G.I. 1958. The Penetration of a Fluid into a Porous Medium or Hele-Shaw Cell Containing a More Viscous Liquid. *Proc R Soc Lond A* **245**: 312–329. https://doi.org/10.1098/rspa.1958.0085

Setu, S.A., Zacharoudiou, I., Daviesa, G.J., Bartoloc, D., Moulinetd, S., Louisb, A.A. Yeomansb, J.M. and Aarts, D. 2013. Viscous Fingering at Ultralow Interfacial Tension. *Soft Matter* **9**: 10599–10605. https://doi.org/10.1039/C3SM51571K

Song, W. and Kovscek, A.R. 2015. Functionalization of Micromodels with Kaolinite for Investigation of Low Salinity Oil-Recovery Processes. *Lab on a Chip* **15**: 3314-3325. https://doi.org/10.1039/c5lc00544b

Tanino, Y. and Christensen, M. 2019. Imbibition Capillary Pressure and Relative Permeability of Mixed-Wet Microporous Rock: New Insights from History Matching. *Transport in Porous Media* **129**: 121–148. https://doi.org/10.1007/s11242-019-01280-4

Tsuji, T., Jiang, F. and Christensen, K.T. 2016. Characterization of Immiscible Fluid Displacement Processes with Various Capillary Numbers and Viscosity Ratios in 3D Natural Sandstone. *Adv. Water Resour.* **95**: 3–15. https://doi.org/10.1016/j.advwatres.2016.03.005

Wang, M. and Leung, J.Y. 2015. Numerical Investigation of Fluid-Loss Mechanisms during Hydraulic Fracturing Flow-Back Operations in Tight Reservoirs. *Journal of Petroleum Science and Engineering* **133**: 85–102. https://doi.org/10.1016/j.petrol.2015.05.013

Wan, J., Tokunaga, T.K., Tsang, C.-F. and Bodvarsson, G.S. 1996. Improved Glass Micromodel Methods for Studies of Flow and Transport in Fractured Porous Media. *Water Resour. Res.* **32** (7): 1955–1964. https://doi.org/10.1029/96WR00755

Wang, Y., Zhang, C., Wei, N., Oostrom, M., Wietsma, T.W., Li, X. and Bonneville, A. 2013. Experimental Study of Crossover from Capillary to Viscous Fingering for Supercritical CO_2–Water Displacement in a Homogeneous Pore Network. *Environ. Sci. Technol.* **47** (1): 212–218. https://doi.org/10.1021/es3014503

Wildenschild, D. and Sheppard, A.P. 2013. X-Ray Imaging and Analysis Techniques for Quantifying Pore-Scale Structure and Processes in Subsurface Porous Medium Systems. *Advances in Water Resources* **51**: 217–246, https://doi.org/10.1016/j.advwatres.2012.07.018

Wilke, S., Guyon, E. and de Marsily, G. 1985. Water Penetration through Fractured Rocks: Test of a Tridimensional Percolation Description. *Math Geol* **17** (1): 17–27. https://doi.org/10.1007/BF01030364

Xu, K., Zhu, P., Huh, C. and Balhoff, M. 2015. Microfluidic Investigation of Nanoparticles' Role in Mobilizing Trapped Oil Droplets in Porous Media. *Langmuir* **31** (51): 13673–13679. https://doi.org/10.1021/acs.langmuir.5b03733

Xu, K., Liang, T., Zhu, P., Qi, P., Lu, Jun., Huh, C. and Balhoff, M. 2017. A 2.5-D Glass Micromodel for Investigation of Multiphase Flow in Porous Media. *Lab on a Chip* **17** (4): 640–646. https://doi.org/10.1039/c6lc01476c

Xu, W., Ok, J.T., Xiao, F., Neeves, K.B. and Yin, X. 2014. Effect of Pore Geometry and Interfacial Tension on Water-Oil Displacement Efficiency in Oil-Wet Microfluidic Porous Media Analogs. *Physics of Fluids* **26**: 093102. https://doi.org/10.1063/1.4894071

Zhang, C., Oostrom, M., Wietsma, T.W., Grate, J.W. and Warner, M.G. 2011. Influence of Viscous and Capillary Forces on Immiscible Fluid Displacement: Pore-Scale Experimental Study in a Water-Wet Micromodel Demonstrating Viscous and Capillary Fingering. *Energy Fuels* **25** (8): 3493–3505. https://doi.org/10.1021/ef101732k

Zhao, B., MacMinn, C.W. and Juanes, R. 2016. Wettability Control on Multiphase Flow in Patterned Microfluidics. *Proc. Natl. Acad. Sci.* **113** (37): 10251–10256. https://doi.org/10.1073/pnas.1603387113

Zhong, J., Abedini, A., Xu, L., Xu, Y., Qi, Z., Mostowfi, F. and Sinton, D. 2018. Nanomodel Visualization of Fluid Injections in Tight Formations. *Nanoscale* **10** (46): 21994–22002. https://doi.org/10.1039/C8NR06937A

Table 1: Summary of micromodel properties.

Model	Pore body width	Pore body depth	Pore throat width	Pore throat depth	Fracture length	Fracture width
M1	200 μm	~21 μm	25 μm	~5 μm	N/A	N/A
M2	200 μm	~21 μm	25 μm	~5 μm	2.2 cm	600, 400, 200μm
M3	200 μm	~21 μm	25 μm	~5 μm	2.5 cm	600μm

Table 2: Summary of fluid properties.

Fluid	Density (g/ml)	Viscosity (cp)	IFT with water (mN/m)
Crude oil	0.92	230	10 ± 0.82
Mineral oil	0.86	170	19 ± 0.97
Water	1.0	1	N/A

Table 3: Summary of the microfluidics experiments considered in this paper.

Model	Oil	Wettability	$Ca_{low} \sim 10^{-7}$	$Ca_{medium} \sim 10^{-6}$	$Ca_{high} \sim 10^{-5}$
M1	Crude oil	Oil wet	Exp. 1, $Ca = 3.5\times10^{-7}$	Exp. 2, $Ca = 3.5\times10^{-6}$	Exp. 3, $Ca = 3.5\times10^{-5}$
	Mineral oil	Water wet	Exp. 4, $Ca = 1.9\times10^{-7}$	Exp. 5, $Ca = 1.9\times10^{-6}$	Exp. 6, $Ca = 1.9\times10^{-5}$
M2	Crude oil	Oil wet	Exp. 7, $Ca = 3.5\times10^{-7}$	Exp. 8, $Ca = 3.5\times10^{-6}$	Exp. 9, $Ca = 3.5\times10^{-5}$
	Mineral oil	Water wet	Exp. 10, $Ca = 1.9\times10^{-7}$	Exp. 11, $Ca = 1.9\times10^{-6}$	Exp. 12, $Ca = 1.9\times10^{-5}$
M3	Crude oil	Oil wet	Exp. 13, $Ca = 3.5\times10^{-7}$	Exp. 14, $Ca = 3.5\times10^{-6}$	Exp. 15, $Ca = 3.5\times10^{-5}$
	Mineral oil	Water wet	Exp. 16, $Ca = 1.9\times10^{-7}$	Exp. 17, $Ca = 1.9\times10^{-6}$	Exp. 18, $Ca = 1.9\times10^{-5}$

Table 4: Summary of measured oil recovery for different geometries.

Ca*	**M1$_{imb}$**	**M2 $_{imb}$**	**M3 $_{imb}$**	**M1$_{dra}$**	**M2 $_{dra}$**	**M3$_{dra}$**
~10^{-7}	0.35	0.36	0.28	0.47	0.33	0.09
~10^{-6}	0.38	0.43	0.15	0.34	0.51	0.10
~10^{-5}	0.40	0.42	0.39	0.52	0.53	0.65

* Capillary numbers are 3.5×10^{-7}, 3.5×10^{-6}, and 3.5×10^{-5} for imbibition, and 1.9×10^{-7}, 1.9×10^{-6}, and 1.9×10^{-5} for drainage.

Table 5: Pore volume injected at 95% recovery in different geometries.

Ca*	**M1$_{imb}$**	**M2 $_{imb}$**	**M3 $_{imb}$**	**M1$_{dra}$**	**M2 $_{dra}$**	**M3$_{dra}$**
~10^{-7}	0.8	4	0.1	9	7	0.1
~10^{-6}	5	14	0.14	1	14	0.1
~10^{-5}	8	25	28	5	54	53

* Capillary numbers are 3.5×10^{-7}, 3.5×10^{-6}, and 3.5×10^{-5} for imbibition, and 1.9×10^{-7}, 1.9×10^{-6}, and 1.9×10^{-5} for drainage.

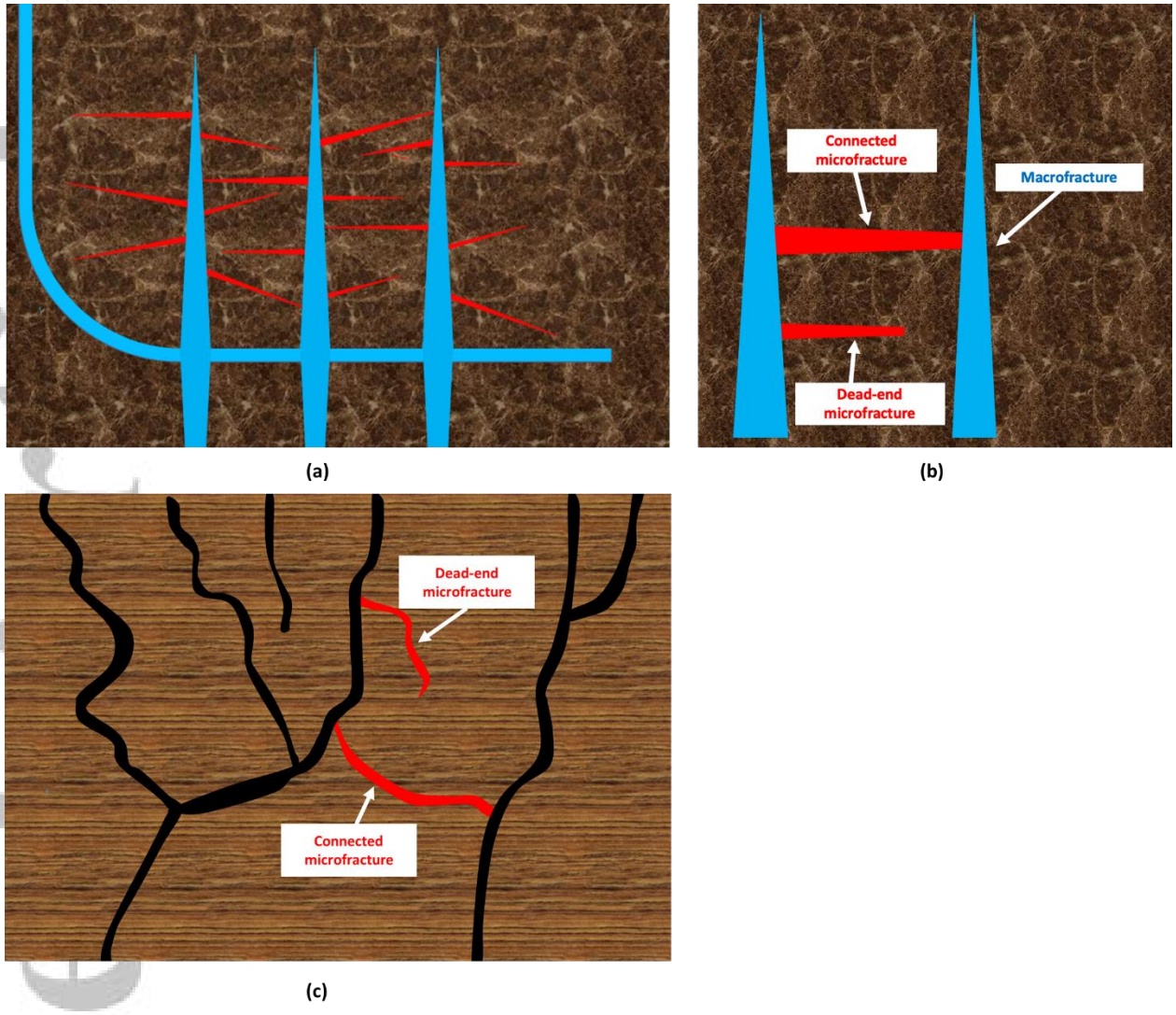

Figure 1. (a) Schematic of a hydraulically fractured horizontal well with microfractures. Macrofractures and microfractures are identified with blue and red, respectively. (b) Close-up schematic of connected and dead-end microfractures. (c) Example of a fracture network in the vadose zone (fracture network conceptualization taken from Faybishenko et al., 2000). Lateral fractures can be considered microfractures for the purpose of the conceptualization of immiscible flow in this paper. Schematics presented here are not to scale and only serve as an illustration for the fracture connectivity classification implemented in this research.

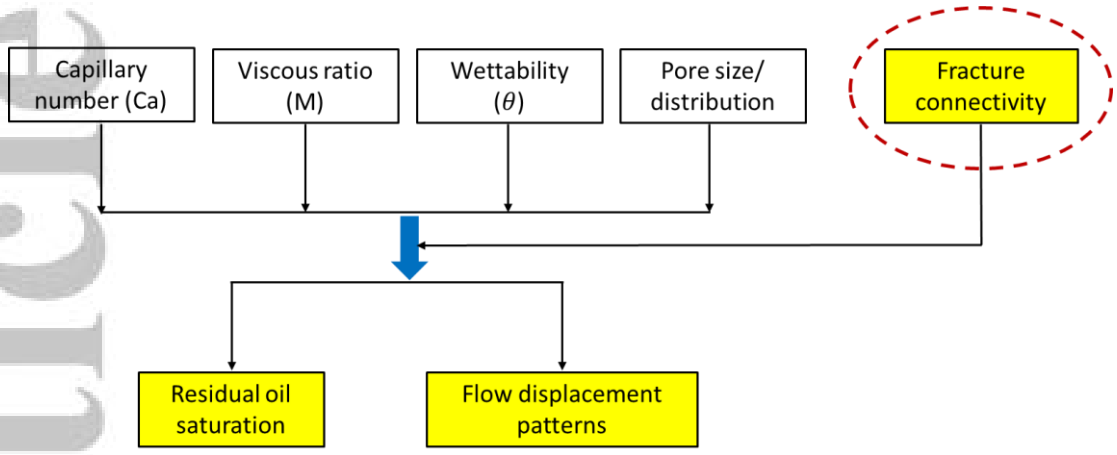

Figure 2. Schematic chart of parameters that affect the behavior of unstable fluid displacement in porous media.

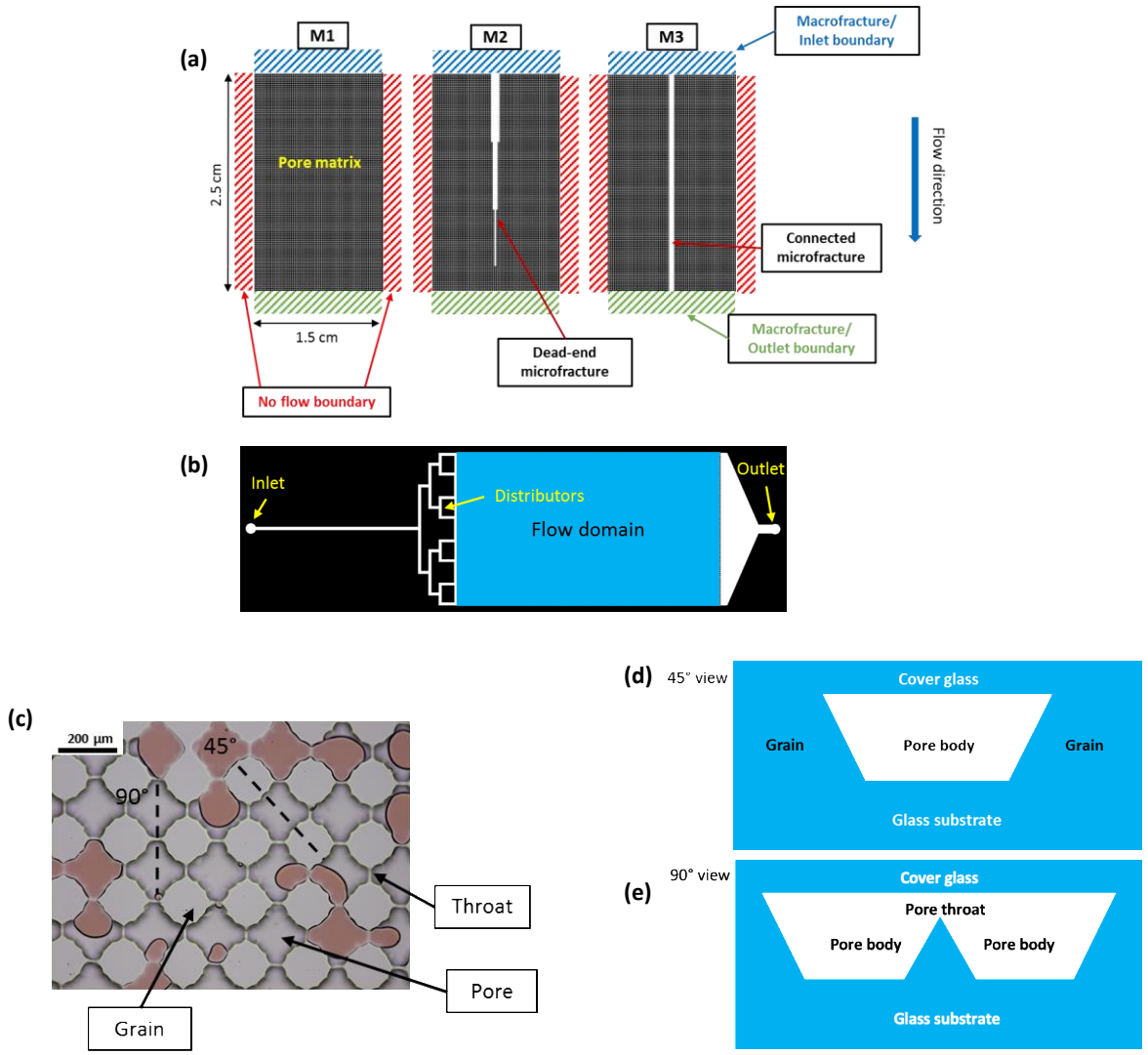

Figure 3. (a) Photomask design of the flow domains in micromodels 1, 2, and 3 denoted as M1, M2, and M3, respectively. (b) Photomask design schematic (M1) of inlet, outlet, flow channels to/from the flow domain. (c) Microscopic image of the micromodel after flow experiment with 45° and 90° cross-sections in planar view. (d) Cross-sectional schematic of micromodel pore body/grain at 45°. (e) Cross-sectional schematic of micromodel pore body/pore throat at 90°. Note that throats are etched shallower than pores as part of the 2.5D fabrication scheme.

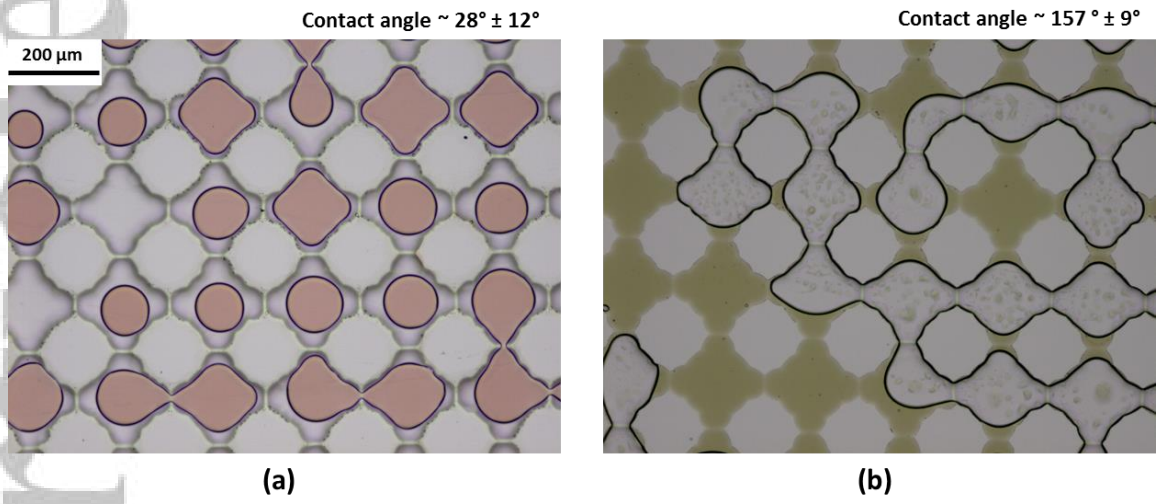

Figure 4. Pore-scale images of (a) mineral oil (red) remaining after water injection in M2, and (b) crude oil (beige) remaining after water injection in M3. Mineral oil and crude oil are the non-wetting and wetting phase, respectively. Contact angles are obtained by measuring along the contact lines at multiple liquids/solid interfaces from corresponding cases.

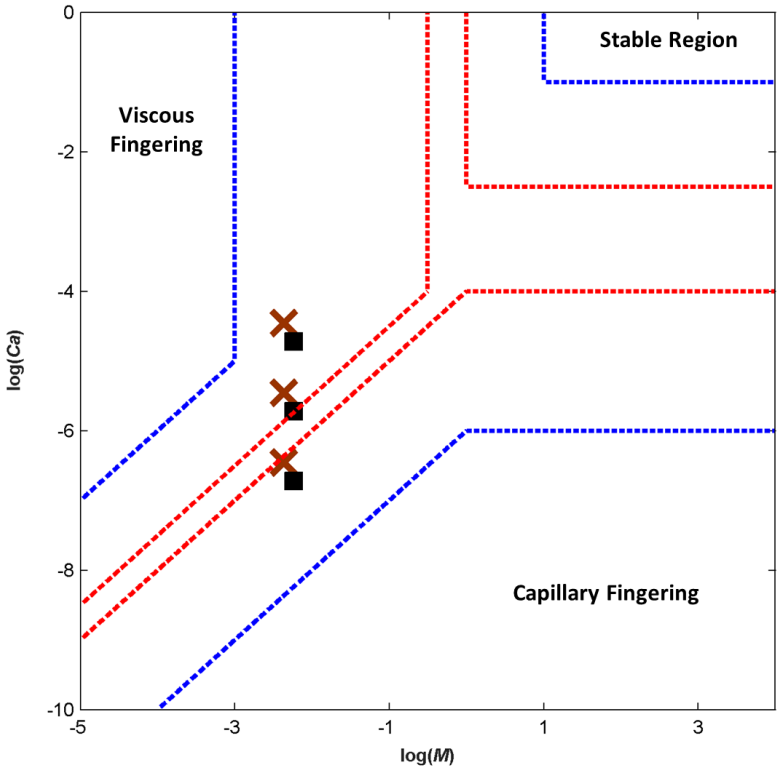

Figure 5. Flow pattern classification based on capillary number (*Ca*) and viscosity ratio (*M*). Boundary lines are determined by Lenormand et al., 1988 (shown in blue) and Zhang et al., 2011 (shown in red). Drainage (crude oil recovery) is identified with black squares while imbibition (mineral oil recovery) is identified with brown X's.

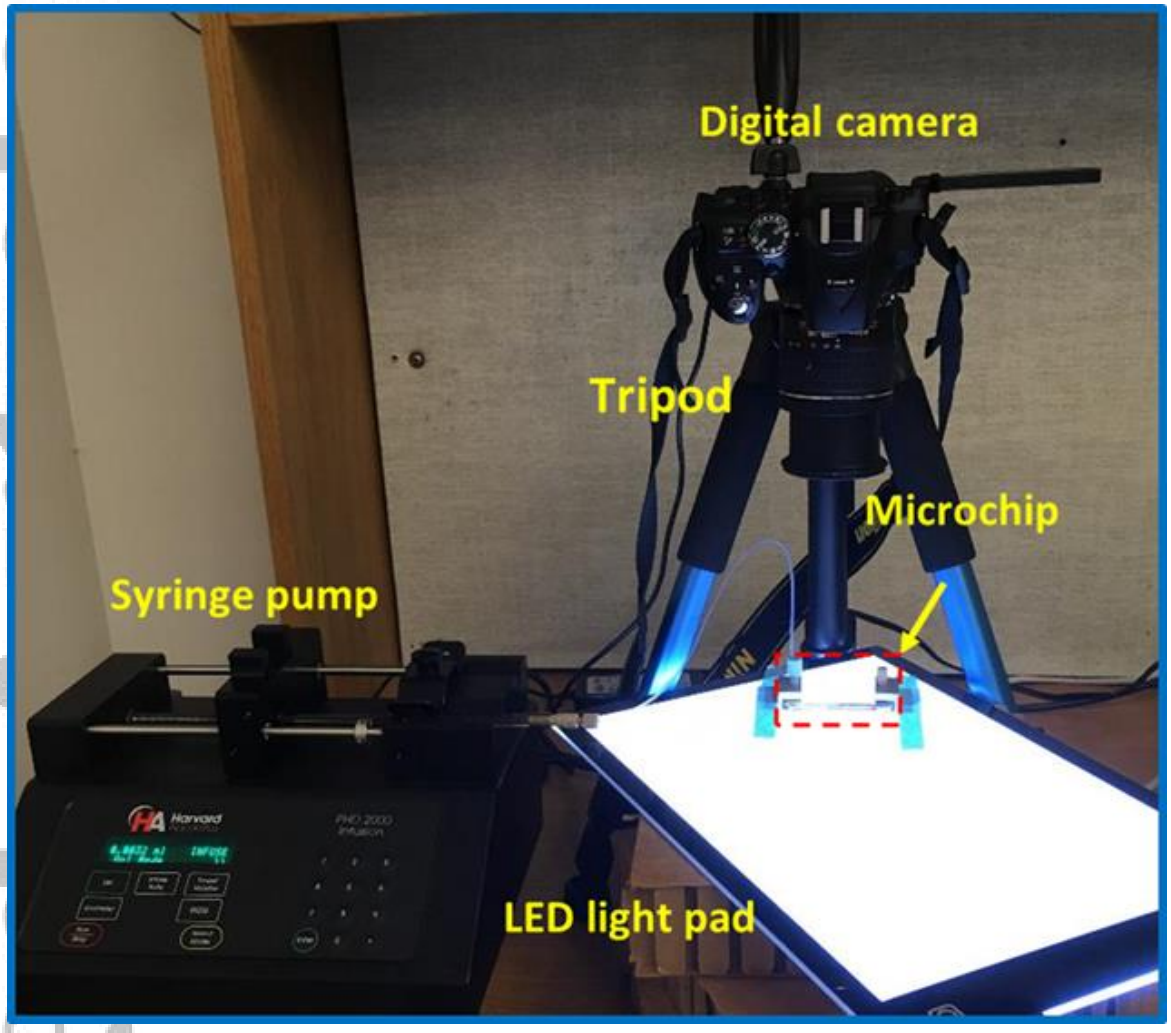

Figure 6. Experimental system, including a digital camera (Nikon D5500), a syringe pump (PHD 2000, Harvard Apparatus), a LED light pad, and a tripod.

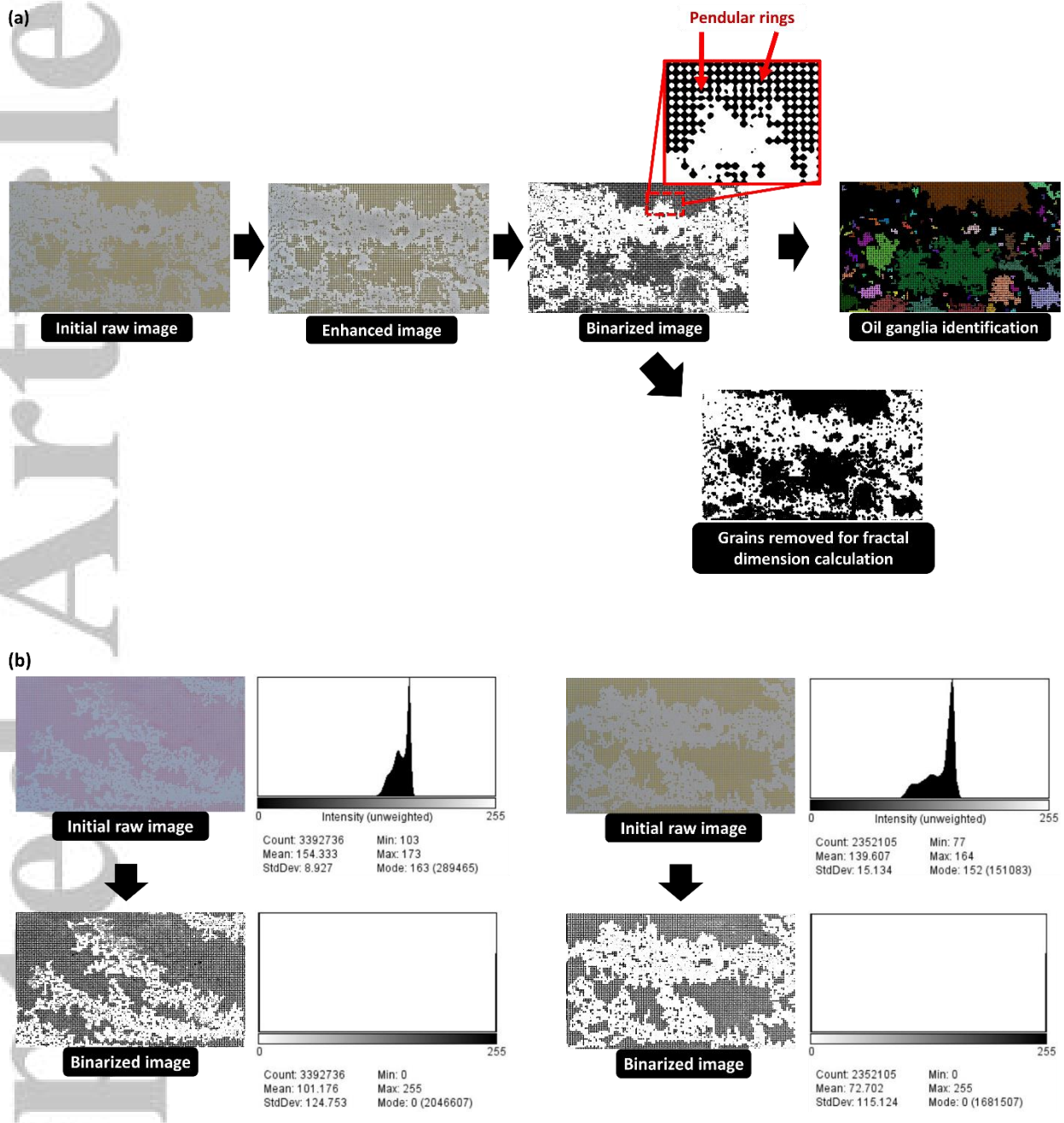

Figure 7. (a) Image processing steps for binarizing each frame and subsequently determining isolated oil ganglia. Note that the steps for image analysis effectively capture wetting-phase pendular rings. (b) Grey scale distribution of the raw and binarized image from imbibition (left) and drainage (right) at *low* capillary number in M1.

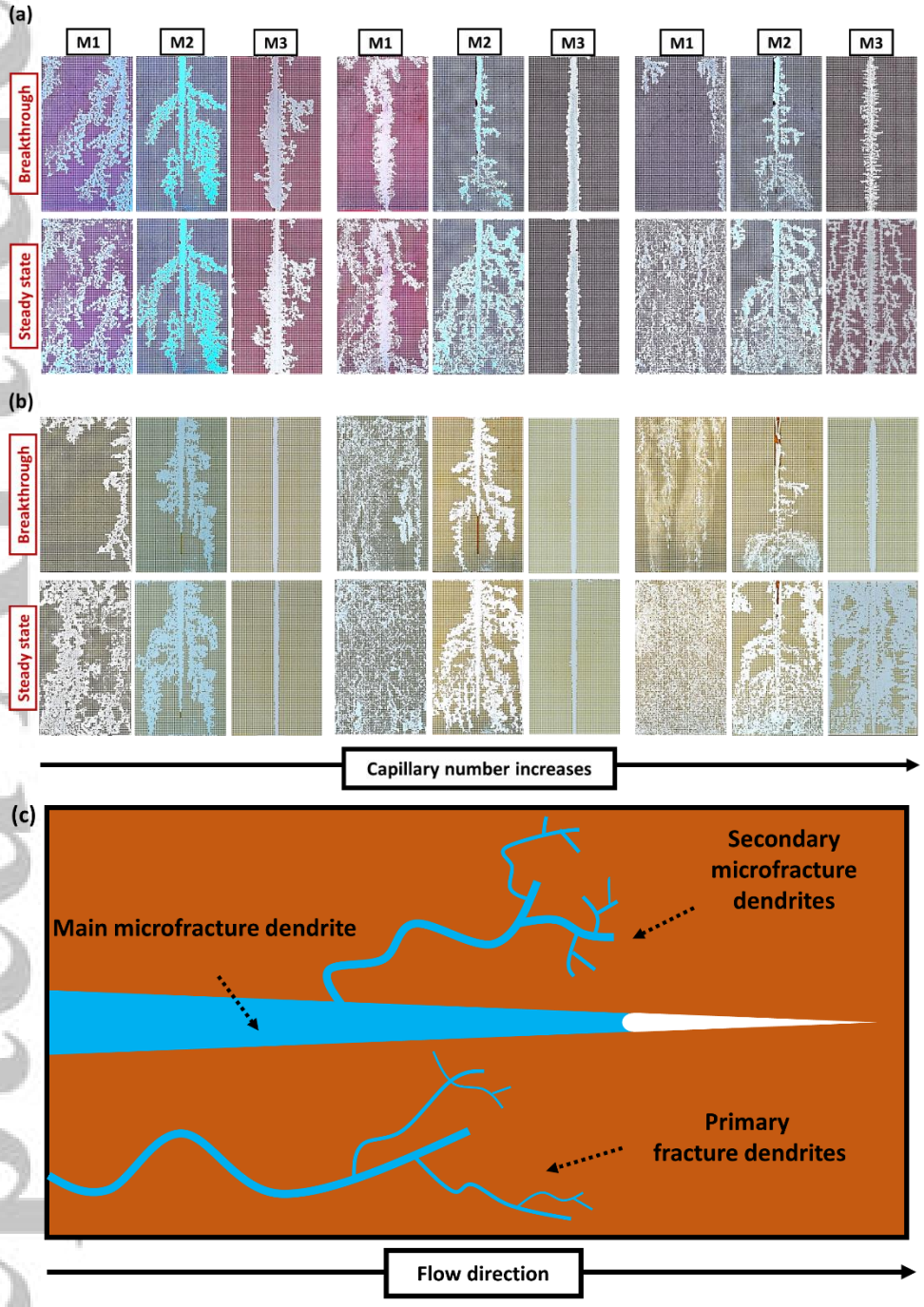

Figure 8. Patterns of invading phase for three capillary numbers at breakthrough and steady state during (a) imbibition, and (b) drainage. The matrix micromodels (M1) demonstrate characteristic that resembles *viscous fingering* behavior by moving towards the outlet and not forming loops. (c) Conceptual picture for fingering fluid dendrite propagation in the presence of a microfracture. Flow direction is from one macrofracture (inlet, not shown) to another (outlet, not shown). Main microfracture dendrites are confined inside the microfracture. Macrofracture dendrites originate from the macrofracture (inlet) and traverse within the matrix. Secondary microfracture dendrites originate from the microfrature and traverse within the matrix.

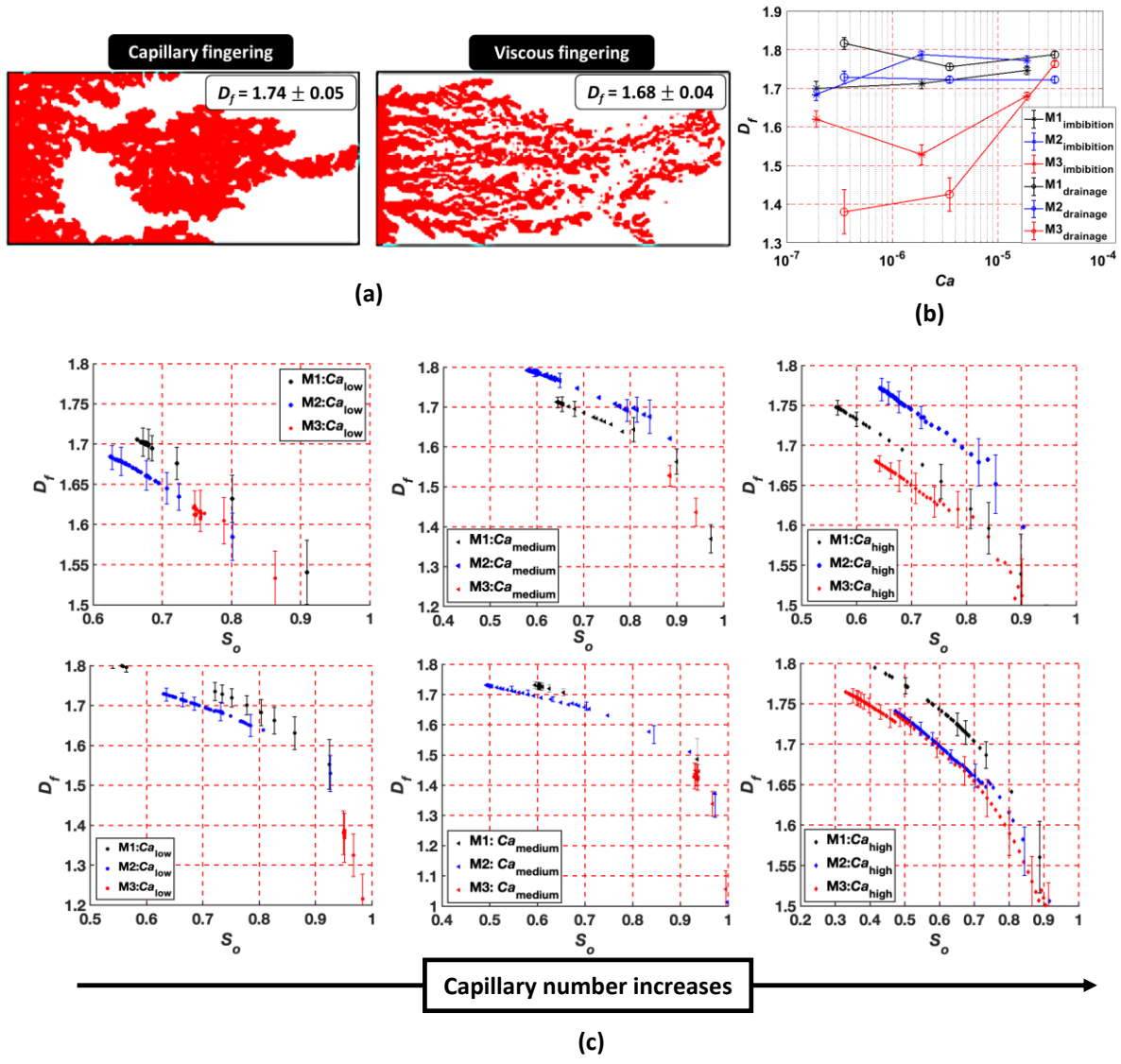

Figure 9. (a) Reference fractal dimension values for capillary and viscous fingering. The higher the fractal dimension, the more coalescent the immiscible front becomes (Chen et al., 2017). (b) Steady-state fractal dimension values calculated for the micromodels at all capillary numbers for the two wettability conditions. (c) Fractal dimension for micromodels throughout their water-flood experiments (top) imbibition and (bottom) drainage. We note that fractal dimension is a function of capillary trapped oil saturation. Error bars are the maximum range of values obtained when values of capillary trapped oil saturation were altered by ±5%.

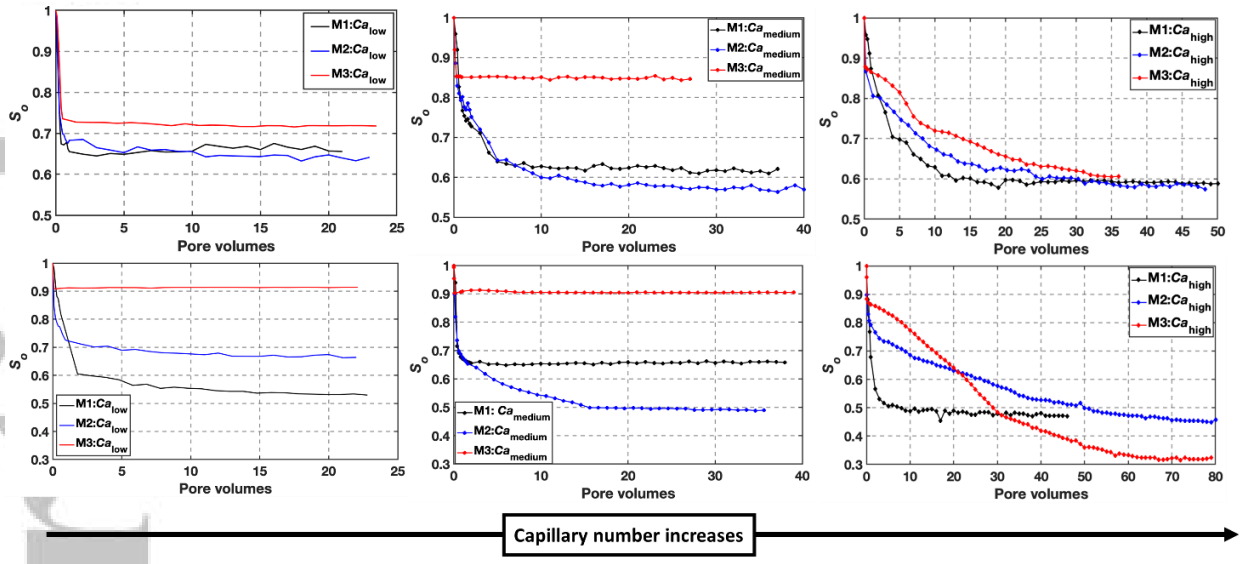

Figure 10. Capillary trapped saturation curves for each micromodel at three capillary numbers during imbibition (top) and drainage (bottom).

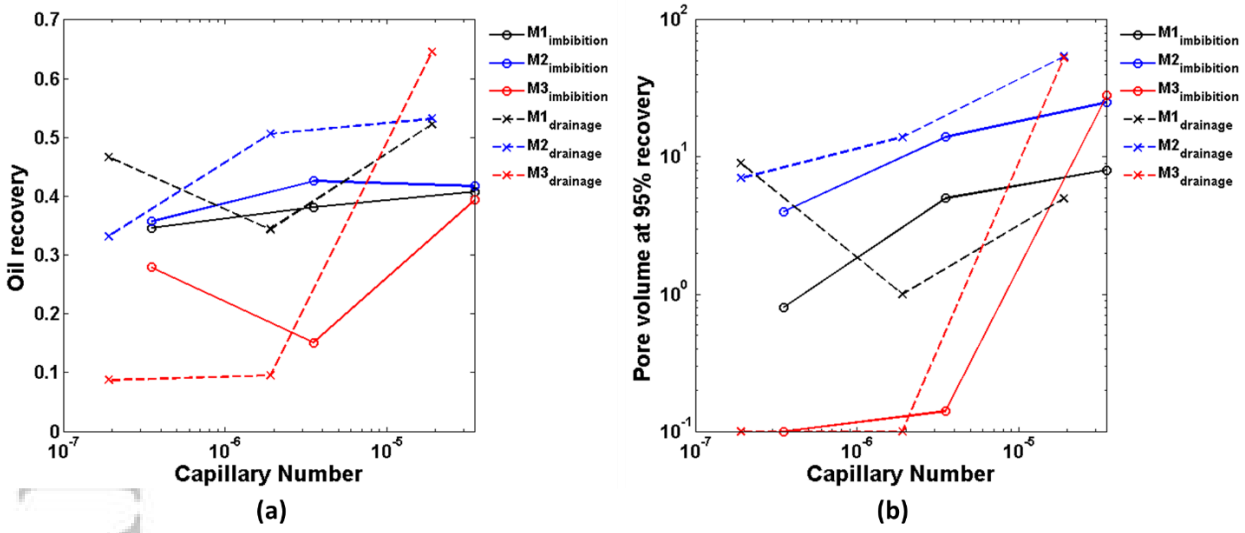

Figure 11. (a) Oil recovery, and (b) pore volume injected at 95% recovery for each micromodel at three capillary numbers for imbibition and drainage processes.

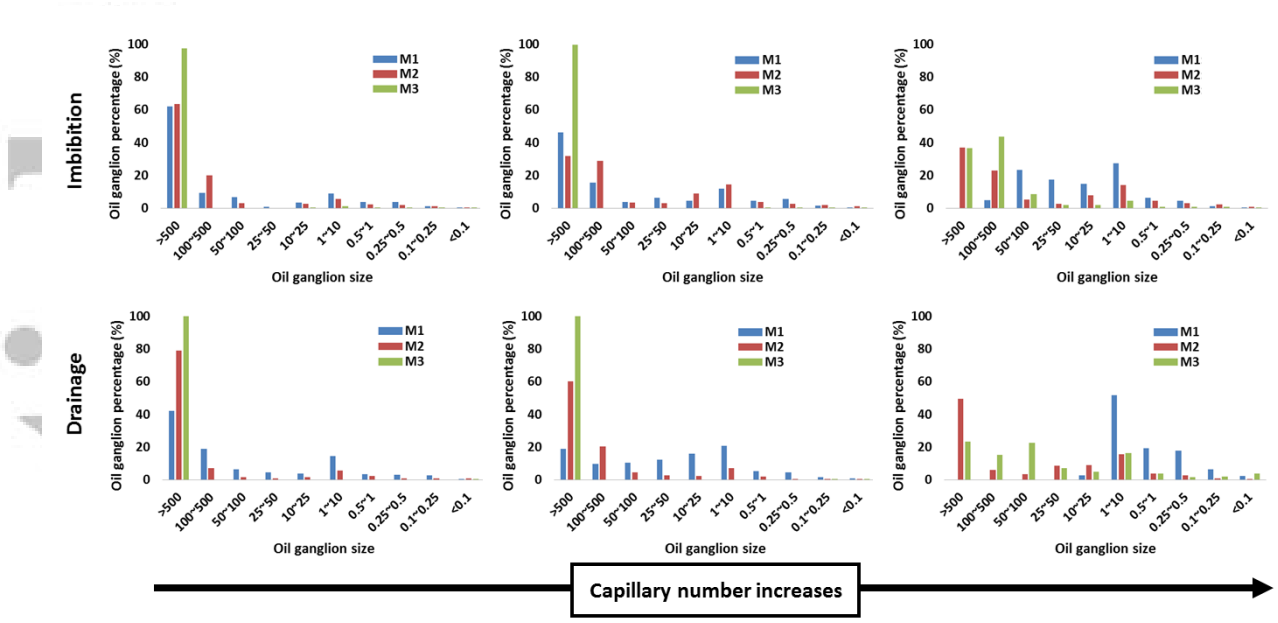

Figure 12. Distribution of oil ganglia at steady state for each micromodel at three capillary numbers during imbibition (top) and drainage (bottom). Oil ganglion size is defined as the actual ganglion size divided by a single pore size. Oil ganglion percentage is defined as the area of a single oil ganglion as percentage of the total remaining oil in each size group.

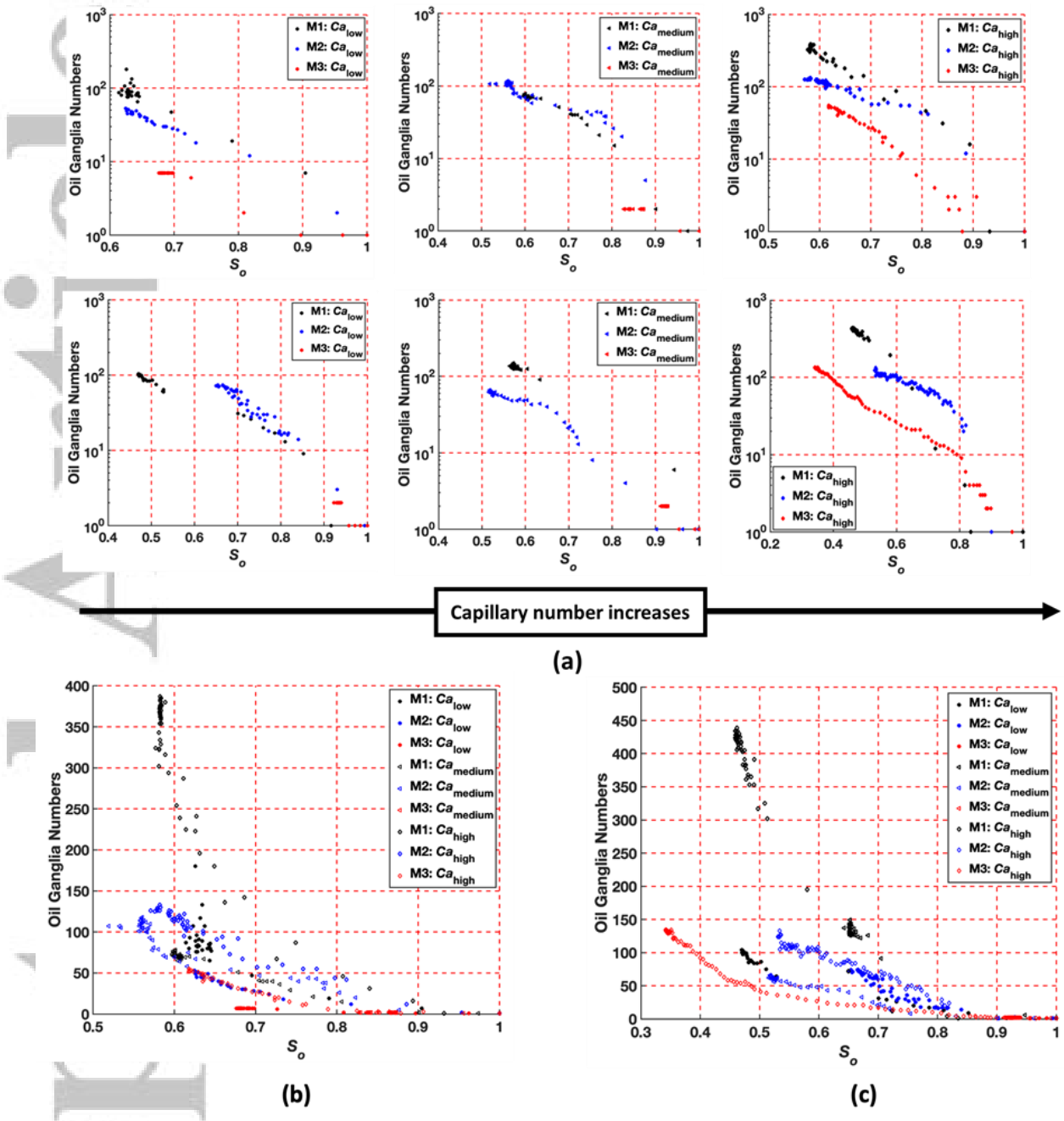

Figure 13. (a) Number of oil ganglia as a function of capillary trapped oil saturation (S_{oil}) for (top) imbibition and (bottom) drainage. Aggregate plots of oil ganglia versus capillary trapped saturation are shown for (b) imbibition and (c) drainage.